





Cite this: *EES Catal.*, 2023,  
1, 874

## Emerging on-chip microcells in electrocatalysis: functions of window and circuit

Jinbo Wang,<sup>†a</sup> Mengyi Qiu,<sup>†a</sup> Yubin Jiang,<sup>†a</sup> Hang Xia,<sup>a</sup> Xiuyun An,<sup>ab</sup>  
 Shuangyin Wang <sup>\*ac</sup> and Yongmin He <sup>\*ac</sup>

An electrocatalytic process that efficiently converts the reactants into high-value-added chemicals has attracted increasing attention in renewable energy fields. Specifically, understanding such a process at a single-material level will be of fundamental importance for catalyst design and mechanism explorations as well. Thanks to the development of electronic devices, on-chip microcells have emerged as a powerful platform through which significant progress has been impressively made. Here, this review provides an overview of the progress based on on-chip microcells. We first introduce how the on-chip microcell develops from electronic transistors like field effect-based and electric double-layer-based ones. Next, we discuss current achievements relying on their two basic functions: the reaction window and the circuit; the former is mainly focused on the active sites, for example, identification of active sites as well as monitoring of their changes; the latter sheds light on its circuit characteristics, such as electrical-field modulation, contact engineering for charge injection, and *in situ* conductance measurement of metallic and nonmetallic catalysts. Finally, we give personal perspectives on this emerging field, including the current challenges and potential applications.

Received 14th July 2023,  
Accepted 4th September 2023

DOI: 10.1039/d3ey00168g

[rsc.li/eescatalysis](http://rsc.li/eescatalysis)

### Broader context

Understanding the catalytic behavior at a single-nanomaterial level is of fundamental importance in electrocatalytic reactions. The on-chip microcell has recently emerged, becoming a powerful tool to attract intensive interest. This review first discusses how the on-chip microcell was developed from an electronic device. Later, we summarize current progress based on their two basic functions: the reaction window and the circuit. Finally, we provide our perspectives on current challenges, such as measurement accuracy and conductance issues, as well as applications, such as reaction extension, model catalysis, a combined strategy, and beyond. This review will arouse widespread interest in the scientific community for an in-depth understanding of the reaction process and, thus, designing high-efficiency catalysts.

## 1. Introduction

To alleviate the ecological and energy-related issues raised from the growing consumption of traditional sources, researchers are seeking potential strategies for developing clean and sustainable energy, such as water splitting for hydrogen energy, fuel cells for electricity energy, and batteries for energy storage.<sup>1–6</sup> Among them, the electrocatalytic reaction, which enables activating or/and converting small molecules (*e.g.*, H<sub>2</sub>O, CO<sub>2</sub>, N<sub>2</sub>, and CH<sub>4</sub>) into high-value-added chemicals (*e.g.*, H<sub>2</sub>, C<sub>2</sub>–C<sub>4</sub> products,

NH<sub>3</sub>, and CH<sub>3</sub>OH) using renewable electricity, has received increasing interest recently.<sup>7–12</sup> Being different from thermo- or photo-catalysis, electrocatalysis usually involves two charge processes: one is the charge flowing from the substrate to the catalyst and then to the catalyst-electrolyte interface; the other is charge transfer at the interface, finally making the reaction happen. Briefly, the former refers to an electronic process where the catalyst should be conductive. The latter refers to a chemical process under which the active sites are usually designed to lower the reaction barrier and improve product selectivity. As a result, it is widely accepted that electrocatalysis is an interdisciplinary field of electronics and chemistry, and not only a “chemical process”.

Current electrocatalysis measurements are mainly based on particle-assembled electrodes in an electrochemical working station (see the setup and structures in Fig. 1). During the electrode fabrication, the catalyst particles are usually spin-coated or dropped on the conductive substrates, such as metal

<sup>a</sup> State Key Laboratory of Chemo/Biosensing and Chemometrics, College of Chemistry and Chemical Engineering, Hunan University, Changsha 410082, P. R. China. E-mail: [shuangyinwang@hnu.edu.cn](mailto:shuangyinwang@hnu.edu.cn), [ymhe@hnu.edu.cn](mailto:ymhe@hnu.edu.cn)

<sup>b</sup> Luoyang Institute of Science and Technology, Luoyang 471023, P. R. China

<sup>c</sup> Greater Bay Area Institute for Innovation, Hunan University, Guangzhou 511300, P. R. China

<sup>†</sup> These authors contributed equally to this work.



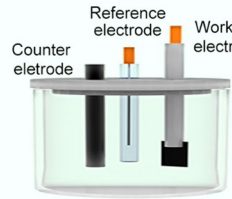
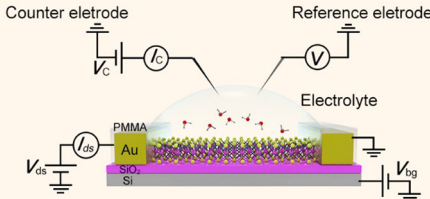
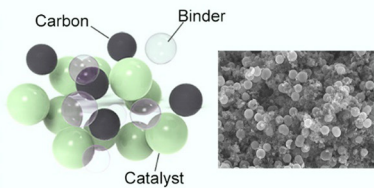
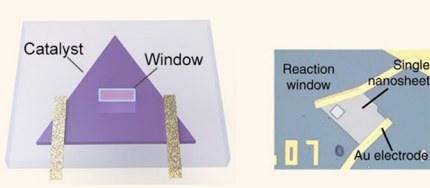
|                      | Particle-assembled electrode  | On-chip microcell  |
|----------------------|---|--|
| Configurations       |    |    |
| Electrode structures |    |    |
| Characteristics      | <p>Complex interfaces<br/>(e.g., catalyst/carbon, catalyst/catalyst, catalyst/substrate, etc)</p> <p>Statistical result<br/>(i.e., average of thousands of samples)</p> <p>Unclear charge-flowing pathway</p> | <p>Identify active sites<br/>(e.g., MoS<sub>2</sub> edge, grain boundary, basal plan etc)</p> <p>Apply external field</p> <p>In-situ monitoring electronic signals.</p> <p>Design catalytic interfaces</p> |

Fig. 1 Comparison of the conventional particle-assembled electrode and on-chip microcell from three aspects: configurations, electrode structure, and characteristics.

film or glassy carbon. Specifically for nonmetallic catalysts, conductive additives, e.g., carbon black, graphene, and carbon nanotubes, are usually induced to improve the conductance of the whole electrode. However, what additives and how much to add is still debated. Generally, for evaluating a given reaction, such a particle-assembled measurement faces three limitations: (i) the statistical average of thousands of samples. The measured data are based on the statistical average of thousands of samples, failing to precisely evaluate the catalytic properties of a single unit (e.g., single nanowire (NW)/nanosheet (NS)); (ii) complexed reaction interface. Conductive additives and binders are usually added during the electrode fabrication process, forming complex interfaces, e.g., catalyst/binder, catalyst/conductive additives, and catalyst/substrate, some of which would cover the catalytic sites or obstruct the ion diffusion;<sup>13–17</sup> (iii) unclear charge-flowing pathway inside the electrodes. It remains a methodological challenge to precisely extract such a pathway using conventional electrochemical impedance spectroscopy (EIS) through a circuit fitting. Based on the above facts, developing effective characterization methods in electrocatalysis is highly desirable.

Along with advancements in micro-/nano-processing technology, an on-chip microcell has recently emerged and become a powerful tool in the electrocatalytic field to probe the catalytic behavior of the electrocatalyst at a single-catalyst level. Significant achievements have been made in such a field in the past nearly ten years, as shown in Fig. 2. For example, Mai *et al.* fabricated a single NW electrode device for *in situ* probing how electrode capacity faded in Li-ion-based energy storage devices,

which is the first microcell example to study the correlation among material structure changes, transport properties, and electrochemical performance.<sup>18</sup> Later, Ding *et al.* turned their attention to electrocatalysis and developed a four-electrode configuration that allows *in situ* monitoring of the surface adsorption/desorption features of metal NWs during the electrochemical process.<sup>19</sup> Besides NW materials, the on-chip microcell was applied to two-dimensional (2D) NS materials. For example, Chowalla *et al.* constructed a low-resistance-contact microcell on monolayer MoS<sub>2</sub> to compare the activity between the edge or basal plane.<sup>20</sup> Similarly, Luo *et al.* set up microcell-combined *in situ* scanning time-resolved microscopy to spatially map the catalytic activity of monolayer MoS<sub>2</sub> during the hydrogen evolution reaction (HER).<sup>21</sup> Notably, such a cell that is derived from a semiconductor device is of particular interest in investigating the electronics-related behavior during the reaction process. For example, C. Frisbie *et al.* applied an electric-field modulation in an HER process.<sup>22,23</sup> Moreover, using *in situ* electronic/electrochemical measurements, our group revealed a universal self-gating phenomenon to clarify the electronic-conduction modulation of >30 semiconducting catalysts during the electrocatalytic reaction.<sup>24</sup> More recently, Duan *et al.* combined EIS and electrical transport spectroscopy (ETS) in a microcell to probe the behaviors of different cations (Li<sup>+</sup>, Na<sup>+</sup>, and K<sup>+</sup>) in HER kinetics.<sup>25</sup>

Based on those achievements, it is timely to provide a review on this field, hopefully attracting more attention for further development in model catalysis. Also, it is noteworthy that some excellent reviews have already been presented in this



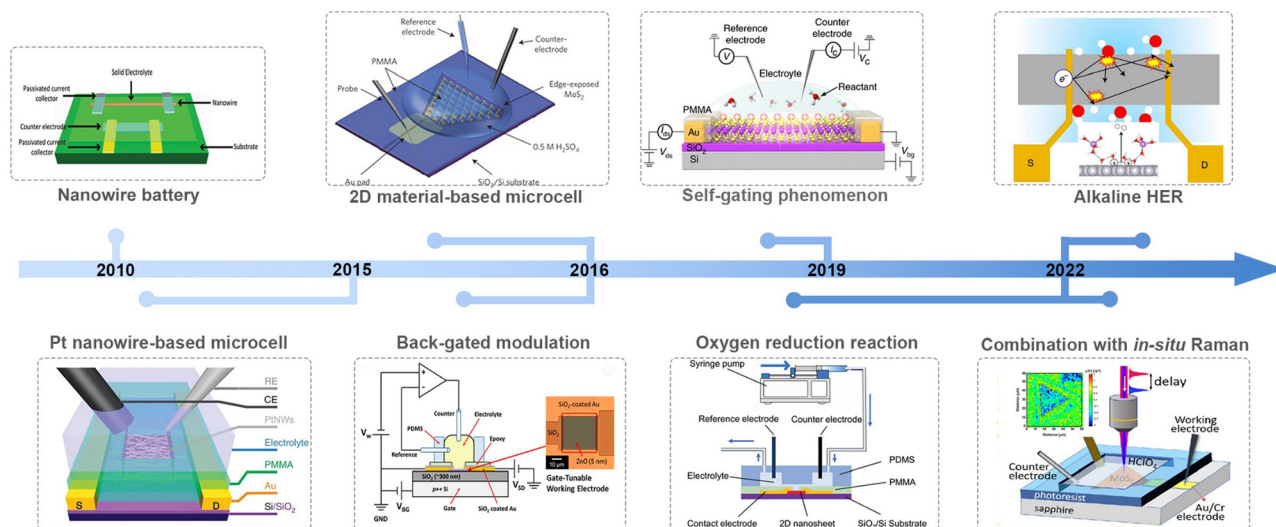


Fig. 2 Development of the on-chip microcell in electrocatalysis.

microcell field; unfortunately, there is still a lack of summaries paying much attention to its electronic characteristics, which is, essentially, derived from a semiconductor electronic device. In this review, we first discuss how the on-chip microcell was developed from an electronic device. Later, we will summarize current progress based on their two basic functions: one is to identify and monitor the active sites through the reaction-window function; the other one, from an electronic standpoint, is the circuit function, such as electrical field modulation, charge injection at the contacts, and *in situ* charge transport/transfer at metallic and semiconducting catalysts. Finally, we provide our perspectives on current challenges and implications in this emergent field.

## 2. Development of an on-chip microcell

This section will discuss how the on-chip microcells have been developed from the top-gated field effect transistors (FETs) and electric double-layer transistors (EDLTs). Both of them contributed to this microcell with well-defined device structures and mature micro-/nano-processing technology, playing a vital role in its emergence and broad applications in electrocatalysis. Given that FETs and EDLTs have been widely used in the electronic fields, while few are known in electrochemistry, their detailed working principles are also discussed in the following.

The emergence of logic transistors in the 1940s dramatically accelerated the development of electronic devices and information systems. In particular, metal-oxide-semiconductor field effect transistors (MOSFETs) have been becoming the cornerstone in those fields.<sup>26–28</sup> Fig. 3a shows the device structure of a typical MOSFET (Fig. 3a), in which the gate voltage is applied through a top electrode, electrostatically tuning the distribution of the charge carriers at the oxide-semiconductor interface.<sup>29–31</sup> The type and density of the charge carriers can

be determined by the sign and magnitude of the voltage applied at the top gate, respectively. As a result, the gate voltage continuously controls the semiconductor's conductance, realizing the smooth switch between “on” and “off” states. Note that, owing to a low dielectric constant of traditional oxides (*e.g.*,  $\sim 10^{-2} \mu\text{F cm}^{-2}$  for 300 nm  $\text{SiO}_2$ ),<sup>32</sup> a large gate voltage is usually needed to realize the above state switch, for example, 10–100 V for the MOSFET based on carbon nanomaterials and metal oxides.<sup>33</sup>

In the 1980s, EDLTs<sup>34,35</sup> that employed an ionic liquid to replace the conventional oxide dielectric were proposed, as illustrated in Fig. 3b. In an EDLT, the applied top-gate voltage (positive) drives the cations toward the semiconductor interface to form an electric double layer (EDL), which can electrostatically modulate the charge carriers of the semiconductor channel.<sup>36,37</sup> Such an EDL can be regarded as a nanogap parallel plate capacitor with a capacitance of up to  $100 \mu\text{F cm}^{-2}$ , much larger than that in MOSFETs.<sup>35</sup> Such a giant capacitance can achieve an ultrahigh carrier accumulation beyond  $10^{15} \text{ cm}^{-2}$  at just several volts, resulting in more effective modulation of charge carriers compared to the above MOSFETs.<sup>38,39</sup> Moreover, such an EDLT has also come out with a new interdisciplinary concept, *i.e.*, iontronics. This bridges electronics and ionics, with broad applications in electrochemistry, solid-state physics, electronic engineering, and biological sciences.<sup>36</sup> For example, Iwasa and colleagues achieved the insulator-metal transition of  $\text{VO}_2$  film by applying just one voltage through EDLTs.<sup>40</sup>

More recently, through introducing an insulating layer and changing the ionic liquid into catalytically-active electrolytes, such as  $\text{H}_2\text{SO}_4$ ,<sup>20,41,42</sup>  $\text{KOH}$ ,<sup>25,43,44</sup> *etc.*, those above EDLTs can be transformed into an on-chip microcell used in the electrocatalytic field (Fig. 3c). One of the most significant advancements is that the introduced insulating layer, *e.g.*, PMMA or  $\text{SiO}_2$ , allows one to selectively expose the region of interest through a window fabricated by the micro-/nano-processing technology, such as e-beam lithography (EBL), for a given



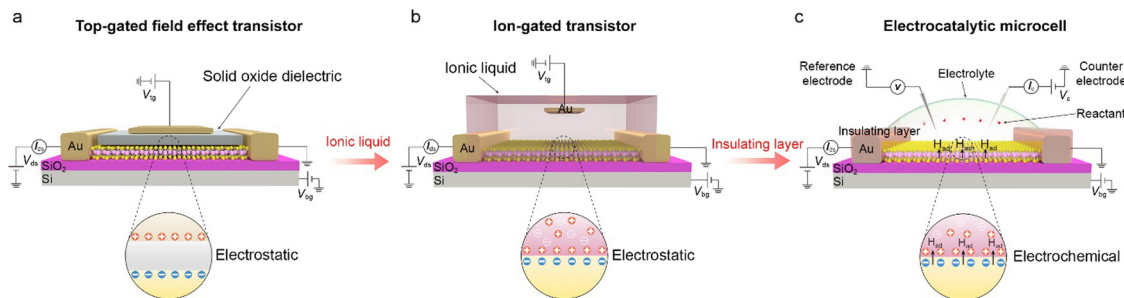


**Fig. 3** Evolution of the on-chip electrocatalytic microcell. (a) Schematic illustration of the top-gated field effect transistor (FET). It is based on a metal–insulator–semiconductor junction, in which the insulator adopts the solid oxide (grey region). When the positive voltage is applied at the top gate (brown region), the negative charge carriers could be induced and accumulate at the oxide–semiconductor interface (grey–yellow region). The carrier concentration depends on the capacitance of the solid oxide and applied voltage. (b) Schematic illustration of the ion-gated transistor, that is, the electric double-layer transistor (EDLT). By changing the solid oxide insulators with a high-mobility ionic liquid, an electric double-layer is formed at the interface, serving as a nanogap parallel plate capacitor with a substantial capacitance (up to  $100 \mu\text{F cm}^{-2}$ ). As a result, applying a low voltage (e.g., 0.1–0.5 V) can achieve high carrier densities (e.g., beyond  $10^{15} \text{ cm}^{-2}$ ), showing more efficiency of conductance modulation. (c) Schematic illustration of the electrocatalytic microcell. Based on the above EDLT structure, the on-chip microcell has been developed by replacing the ionic liquid with reactive electrolytes (e.g.,  $\text{H}_2\text{SO}_4$ ,  $\text{HClO}_4$ , phosphate buffer saline, and  $\text{KOH}_2$ ) and introducing an insulating layer (such as PMMA, photoresist, or  $\text{SiO}_2$  films) to make the reaction windows. The counter and the reference electrode are also used to normalize the reaction voltage to the standard electrochemical potential. Regarding those developments, such a cell exhibits two basic functions: reaction window and circuit, corresponding to an electrochemical view as well as an electronic view, respectively.

reaction. Such a window enables various electrocatalytic reactions to only occur in the region of interest and obviate the leakage current from the metal electrodes. Benefiting from the reaction window, the precise micro-area measurement is achievable through the on-chip microcell, which helps to investigate the active sites in electrocatalysis.

Following the above timeline, two points need to be noted here for comparing on-chip microcells with the above electronic transistors, as follows:

One is the leakage current generated from the gating electrode in the electronic transistors. As is well-known, it must be avoided; on the contrary, such a current is needed for the on-chip microcell, which corresponds to the signal of the catalytic reaction (*i.e.*, the charge transfer process). Taking the HER process as an example, the leakage collected in a microcell is that the reactants ( $\text{H}_3\text{O}^+$ ) receive the electrons at the active sites and generate the adsorbed hydrogen atoms ( $\text{H}_{\text{ad}}$ ).<sup>45</sup>

The other one is conductance modulation arising from EDL. The EDL widely exists in both EDLT and on-chip microcells; in the former, EDL can effectively modulate the conduction of the channel. Similarly, in the latter, it can also modulate the nonmetallic catalysts (conductive or even insulated). Therefore, an *in situ* conductance evaluation should be performed in on-chip microcells to verify whether the microcell works during the measurements. However, such an evaluation is usually neglected in the current microcell measurement.

### 3. Fabrications and characteristics of on-chip microcells

Fig. 4 shows the typical fabrication procedures of on-chip microcells, with 2D TMD material as an example. First, a  $16 \text{ mm} \times 16 \text{ mm}$   $\text{SiO}_2$  (285 nm)/Si chip with pre-patterned

32 or 16 Au contact pads was fabricated using conventional photolithography followed by thermal evaporation. Second, CVD-grown or mechanically exfoliated 2D catalysts were transferred onto the chip. Subsequently, an EBL process, followed by thermal evaporation, was used to fabricate the drain and source metal contacts (Cr/Au or Ti/Au). Finally, the whole chip was passivated by  $1 \mu\text{m}$ -thick PMMA film, and a second EBL process was adopted to carve windows on the catalytic region. As a result, spatial control of the electrocatalytic reaction was achieved through such a PMMA-passivated window, which ensured that the reaction only occurred in the region of interest.

Currently, the signals collected from the on-chip microcells are usually several or tens of nA, thus putting forward a high precision requirement for the electrochemical workstation. For example, to obtain a smooth Tafel slope in the HER, the background noise current should be kept as low as  $10^{-11} \text{ A}$ . Alternatively, high-precision source measurement units (SMUs) could also be used to meet such a requirement. Here, we took an *in situ* electronic/electrochemical measurement in our lab as an example for a detailed introduction; please see the testing environment and setup in Fig. 5. First, four electrodes were used, including microcell graphite and an Ag/AgCl micro-reference as the counter and reference, and the other two electrodes as the working electrodes connected to the catalysts (as the source and drain contacts to collect the *in situ* electronic signals during the electrocatalysis). Second, in our setups, two source measurement units (SMU), *i.e.*, SMU 1 (Keithley 2400) and SMU 2 (Keithley 2450), were used instead of traditional electrochemical workstations. Their equivalent circuit diagram is presented in Fig. 5. In SMU 1, the “High Force (Force HI)” and “Low Force (Force LO)” are connected to the source and drain electrodes on the catalyst for the electronic measurement ( $I_{\text{ds}}$ ). In SMU 2, both “Low Force (Force LO)” and “Low Sense



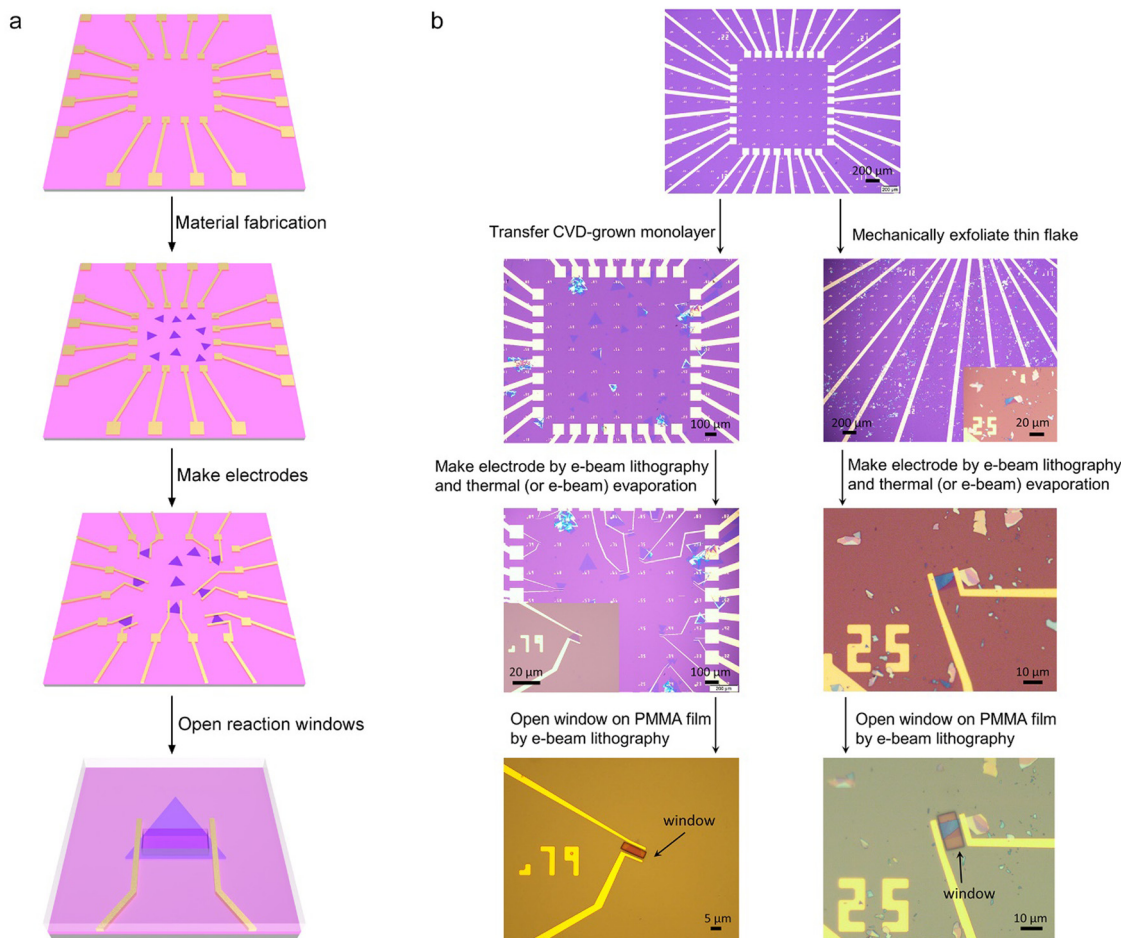


Fig. 4 Fabrication process of an on-chip microcell. (a) Schematic illustration of the fabrication steps of the on-chip microcell. (b) Typical fabrication procedures in 2D TMD-based microcells, in which CVD-grown and mechanically-exfoliated samples were introduced, respectively.

(Sense LO)” terminals are connected with the working electrode, and the “High Force (Force HI)” and “High Sense (Sense HI)” terminals were connected to the counter electrode and reference electrode for the electrochemical measurement ( $I_c$ ). These two measurements are synchronized by the general-purpose interface bus (GPIB) and the Labview script, allowing simultaneous recording of the electronic and the electrochemical signals.

Taking the above advantages, such an on-chip microcell presents several fantastic features (see Fig. 1), including (i) identifying the active sites through reaction windows. Such a window is able to expose regions of interest on a catalyst using an insulation layer (such as PMMA); (ii) regulation of the reaction through applying an external electrical field. Based on a field-effect-transistor circuit, such a microcell also enables regulating the electrochemical reaction, *e.g.*, activity or interface, by applying an electrical field using a back gate voltage; (iii) *in situ* monitoring electronic signals. Derived from a semiconductor electronic device, such a cell can *in situ* probe the conductance of the catalyst during a reaction process. Finally, (iv) design of the catalyst interface. Using the micro-/nano-processing technology, various heterostructure interfaces, such as bottom-/top-electrodes,

and interfinger electrodes, could be designed. Thanks to those features, several interesting functions have been derived, contributing to an extensive development of microcells in electrocatalysis, which will be discussed in the following.

## 4. Functions of on-chip microcells

In this section, we will discuss current achievements on on-chip microcells through paying attention to their two basic functions: the reaction window and the circuit. The reason why we made such a classification is based on the interdisciplinary behavior of on-chip microcells, that is, the combination of electrochemistry and electronics. On the one hand, with the assistance of the reaction window, microcells can be used to study the active sites, such as identifying what they are as well as monitoring how they change. On the other hand, derived from the FET or EDLT circuits, they enable investigating the reactions from an electronic point of view, such as external electrical field modulation, contact engineering for charge injection, and *in situ* conductance measurement of metallic and nonmetallic catalysts.



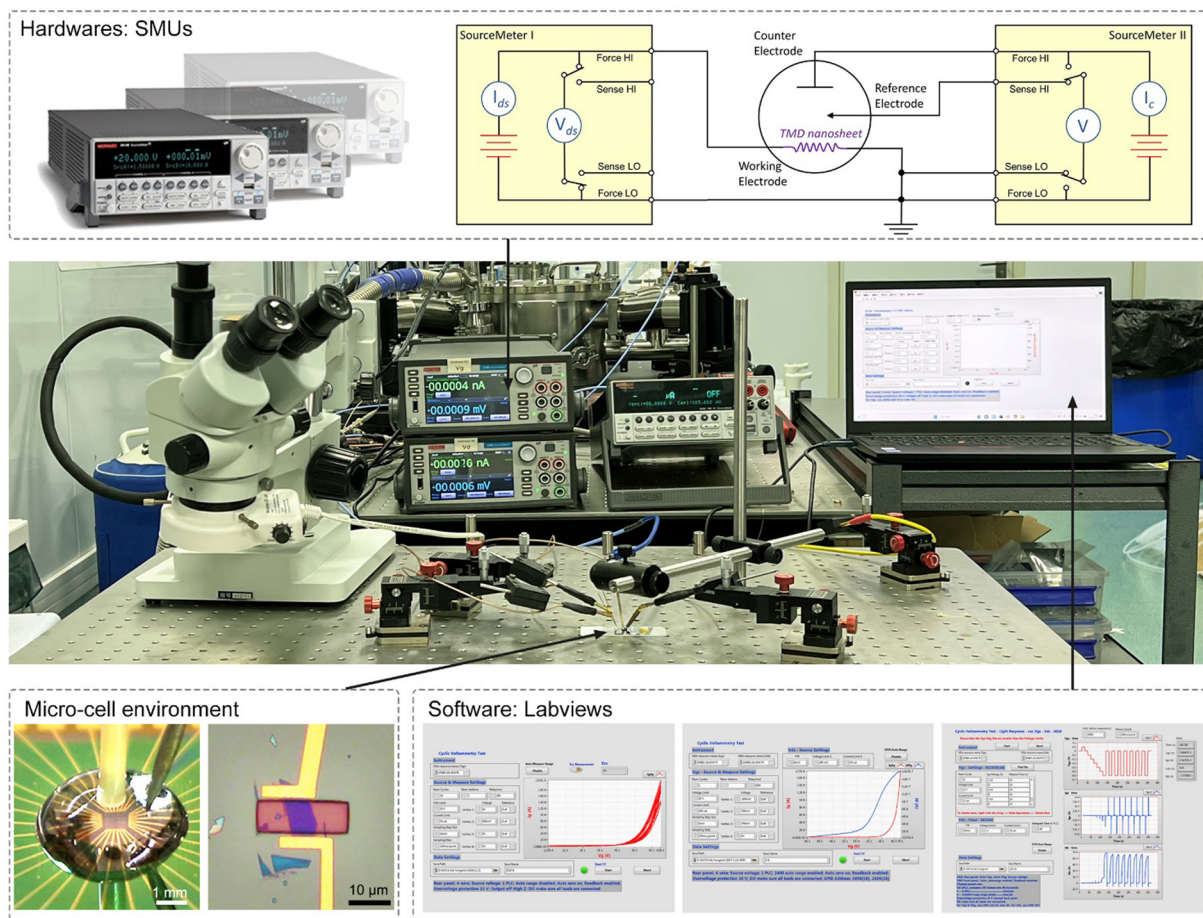


Fig. 5 The typical testing setups used in our lab. The hardwares involved in the test are source measurement units (SMUs), and the software is Labview. Taking *in situ* electronic/electrochemical measurement as an example, SMU 1 and SMU 2 are used for the electronic and the three-electrode electrochemical measurements, respectively, as the equivalent circuit diagram shows.

#### 4.1 Reaction window

In an on-chip microcell, the reaction window is carved by EBL on a PMMA-covering layer, capable of exposing regions of interest at a micro-size for a given electrocatalytic reaction. Thanks to such a window, this cell provides a promising platform to identify the active sites and monitor their changes at a single-material level, which is crucial for the rational design of excellent catalysts as well as the exploration of the mechanism behind the reaction.

**4.1.1 Identification of active sites.** In the past decade, 2D transition metal dichalcogenides (TMD/TMCs/TMDCs), as exemplified by MoS<sub>2</sub>, have attracted considerable interest in water splitting. This is attributed to their atomically thin nature that can act as an interface with the possibility of maximum exposure of nearly all active sites to the reaction. Importantly, how to identify the potential active sites in TMDCs is extremely necessary to enhance the electrocatalytic activity. Intrigued by the above window behavior, the microcell has successfully identified various active sites such as phases,<sup>46,47</sup> grain boundaries (GBs),<sup>48,49</sup> edges,<sup>50,51</sup> doping,<sup>52–54</sup> and so on (Fig. 6a), which is in favor of designing high-efficiency catalysts in electrocatalysis.

**Phases.** The phases have a profound effect on the catalytic properties and the conductivity for 2D TMDCs. For example, 2H-phase MoS<sub>2</sub> is relatively stable while electrochemically-inert; on the contrary, its 1T-phase or 1T'-phase counterpart present metallic behavior with a better HER activity.<sup>55,56</sup> However, since they usually mix in a sample, it is challenging for the conventional particle-assembled electrodes to distinguish the intrinsic activity of each phase. Aiming at solving this issue, Jiao and co-workers synthesized a 1T'-MoS<sub>2</sub> monolayer with high purity and crystallinity through a potassium (K)-assisted chemical vapor deposition (CVD) method, and then compared its activity with the 2H-phase counterpart using a microcell. It can be seen from Fig. 6b that 1T'-MoS<sub>2</sub> exhibits higher catalytic performance than its counterpart, which is attributed to the efficient electrical coupling between the substrate, rapid electron transport, and increased catalytic active sites as well.<sup>57</sup>

**GBs.** As one of the line defects, GBs are universally found in 2D materials. Using the on-chip microcell, the activity of a single GB can also be detectable. For example, Liu and co-workers compared the HER activity among a single GB, a single edge and the basal plane.<sup>48</sup> The results showed that the GB had



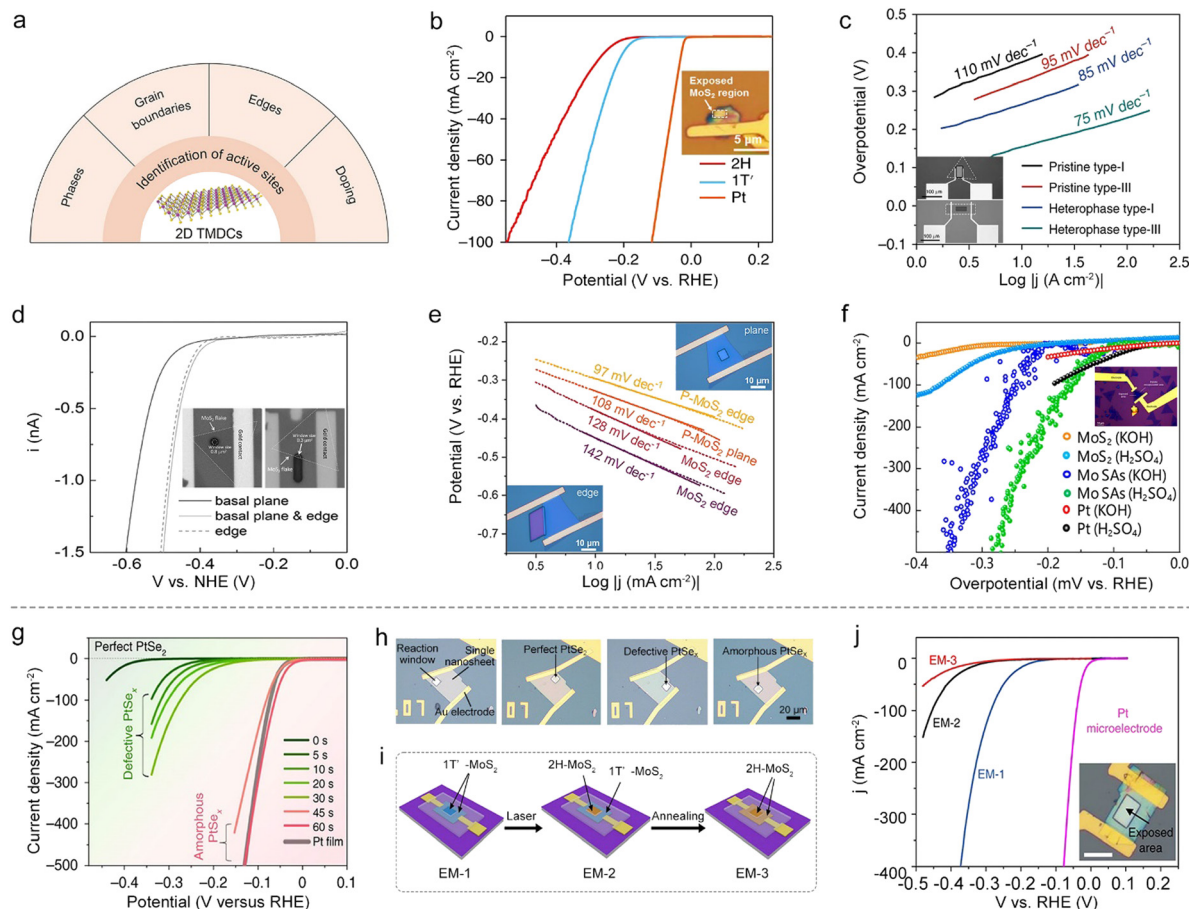


**Fig. 6** Identifying active sites and monitoring their changes at a single material. (a) Various active sites for 2D TMDCs identified by on-chip microcells. (b) Polarization curves of Pt, 1T'-MoS<sub>2</sub> and 2H-MoS<sub>2</sub>. Inset: The optical image of the microcell. (c) Tafel plots of MoS<sub>2</sub> with different types of domain boundaries. Inset: The optical images corresponding to the single-crystal MoS<sub>2</sub> microcell without 2H–2H domain boundaries and the polycrystalline MoS<sub>2</sub> microcell with domain boundaries. (d) Polarization curves of the MoS<sub>2</sub> basal plane with and without edge active sites. Inset: The optical images of MoS<sub>2</sub> microcells with exposed edges and basal planes. (e) Tafel plots of the basal plane and edge sites. Inset: The optical images of a P-MoS<sub>2</sub> microcell with exposure of the edge and the basal plane. (f) Polarization curves of MoS<sub>2</sub>, Mo SAs sitting on cogenetic MoS<sub>2</sub> (Mo SAs/ML-MoS<sub>2</sub>) and Pt. Inset: The optical image of the microcell. (g) Polarization curves of the PtSe<sub>x</sub> NS with a 0 to 60 s treatment duration. (h) Optical images of PtSe<sub>x</sub> microelectrodes with reaction windows through different plasma treatment times. (i) Schematic of the fabrication of three types of electrochemical microcells (EM-1, EM-2, and EM-3) via a phase-transition strategy. (j) Polarization curves of EM-1, EM-2 and EM-3. Inset: The corresponding optical image of EM-1.

better activity than the edge and basal plane. To further make use of such a GB site, the authors demonstrated the synthesis of wafer-size TMD films with an ultra-high density of GBs (up to  $10^{12} \text{ cm}^{-2}$ ). Those films showed an excellent hydrogen evolution performance (onset overpotential,  $\eta_{\text{onset}}$ : 25 mV and Tafel slope:  $54 \text{ mV dec}^{-1}$ ), thus indicating an intrinsically high activation of the TMDC basal plane.

On the other hand, besides the above homo-phase ones, homo-phase GBs can also be fabricated using phase engineering, whose improved activity could be verified by microcells. For instance, Zhang and co-workers utilized an on-chip microcell to investigate the HER activity between 2H–2H homo-phase and 2H–1T hetero-phase ones in MoS<sub>2</sub>, as shown in Fig. 6c. Compared with pristine type-I and type III samples (2H–2H homo-phase GBs), an improved catalytic performance was observed in the 2H–1T hetero-phase, which is ascribed to the metallic 1T-phase offering better charge transport capacity than

the 2H-phase.<sup>58</sup> Alternatively, Yang *et al.* recently studied the activity of hetero-phase GBs between the 2H-phase and 1T'-phase in MoTe<sub>2</sub> films. The microcell measurement showed a clear improvement of HER activity for 2H–1T' hetero-phase GBs compared with the pristine MoTe<sub>2</sub>. This is the result of their local electronic structure and their unique covalent nature.<sup>49</sup>

**Edges.** The edges of 2D TMDCs with an unsaturated coordination environment are usually electrochemically active. For example, through the selective exposure of the edge in an on-chip microcell, Lou and co-workers have examined its HER activity in 2H and 1T'-MoS<sub>2</sub> monolayers. Moreover, the linear sweep voltammetry (LSV) curves in Fig. 6d showed that the edge gave a much higher HER activity than that of the basal plane.<sup>50</sup> Beyond the MoS<sub>2</sub> catalyst, the microcell is also applicable for identifying the activity of edge sites for other 2D materials, such as WTe<sub>2</sub> and PtSe<sub>2</sub>. For instance, Cha *et al.* investigated the



activity of (010) and (100) edges of  $\text{WTe}_2$  in an on-chip microcell. The results demonstrated that the (100) edge was more active, which could be correlated to its lower Gibbs free energies of hydrogen adsorption ( $\Delta G_{\text{H}^*}$ ) than that of the (010) edge.<sup>59</sup> Subsequently, Jiao *et al.* probed the HER activity of the  $\text{PtSe}_2$  edge by using a microcell to expose the edge and basal plane selectively. The edge also showed much higher catalytic performance, similar to the above examples of 2D  $\text{MoS}_2$  and  $\text{WTe}_2$ .<sup>51</sup>

**Doped atoms.** Owing to the abundant valence states and flexible oxidation capabilities, doping atoms, such as B,<sup>60</sup> F,<sup>61</sup> N,<sup>62</sup> P,<sup>54,63</sup> and Mo,<sup>64</sup> can also enhance the HER activity of 2D materials. More recently, Ye *et al.* studied the edge effect of phosphorus (P) doping on a  $\text{MoS}_2$  NS (Fig. 6e). The Tafel curves indicated that the P- $\text{MoS}_2$  edge had the lowest Tafel slope among those samples, as a result of its lower hydrogen adsorption energy and hydrogen evolution activation barrier.<sup>54</sup> Apart from nonmetal doping of TMDCs, metal doping has also been extensively studied to activate the basal plane of TMDCs. For example, Liu and co-workers utilized a cold hydrogen plasma reduction method to synthesize Mo-single-atom doped  $\text{MoS}_2$ , as shown in Fig. 6f. The microcell measurements show that such a catalyst shows more exceptional intrinsic activity with an overpotential of 261 mV and 209 mV at  $10 \text{ mA cm}^{-2}$  in 0.5 M  $\text{H}_2\text{SO}_4$  and 1.0 M KOH, respectively. The authors claimed that the improved performance is a consequence of the increase of the bond strength through hybridization, leading to fast hydrogen adsorption/desorption kinetics and superior hydrogen evolution activity.<sup>64</sup>

**4.1.2 Monitoring the change of active sites at a single material.** Benefiting from mature micro-/nano-processing technology, the on-chip microcell can monitor the change of active sites at a single-material level. Such a level would eliminate the extra factors frequently observed in macro-electrodes (*e.g.*, complex interfaces and a mixture of various sites), thus allowing high-precision monitoring of the change of active sites.

A typical example is that Liu *et al.* adopted plasma treatment to obtain desired regions, *e.g.*, perfect single-crystal, defective single-crystal, and amorphous  $\text{PtSe}_x$  on a single  $\text{PtSe}_2$  NS, for a fair comparison among their HER activities. Fig. 6h shows the optical images of those microelectrodes with different reaction windows, and the electrocatalytic performances of these regions are summarized in Fig. 6g. It is worth mentioning that an abruptly improved performance was observed in the microcell, solely corresponding to the transition of the catalytic site during this etching process, that is, from Se vacancies to the amorphous Pt sites. Such a finding gave direct evidence of how the active sites changed during the etching process.<sup>10</sup> Similarly, Zhai and co-workers precisely controlled the oxidation degree at a single  $\text{MoTe}_2$  NS by the varying processing times with  $\text{O}_2$  plasma. Using an on-chip microcell, they carefully monitored the changes of active sites under defect engineering. The experimental results first verified a high onset overpotential of 280 mV for the pristine  $\text{MoTe}_2$  NS, showing a nearly HER-inert activity. Impressively, as the  $\text{O}_2$ -plasma treatment time

extended, a linear decrease of the onset overpotential of the oxidized  $\text{MoTe}_2$  was observed, and such a linear behavior was solely ascribed to the oxygen vacancies that increased the surface charge and reduced  $\Delta G_{\text{H}^*}$ .<sup>65</sup>

Besides the above factors, the TMDC thickness can also affect the catalytic properties, which the on-chip microcell could precisely monitor. For example, Jiao *et al.* studied the influence of  $\text{PtSe}_2$  thickness on the HER activity at a single NS using the on-chip microcell. In the experiment, the authors firstly made a single-crystalline 2D  $\text{PtSe}_2$  NS with a controlled number of layers, and then probed the HER activity at the thickness-varied regions through the reaction window. Note that, such a measurement allowed a precise evaluation of the activity change only originating from the thickness effect. Finally, in conjunction with theoretical calculations, they clearly demonstrated how the number of layers affected the active sites of 2D  $\text{PtSe}_2$  NSs and correspondingly altered their HER performances.<sup>51</sup>

Beyond a sole factor, the on-chip microcell can further monitor multiple factors affecting the catalytic reaction. A typical example is that Zhang and co-workers conducted phase-dependent HER studies in electrochemical microcells. In their experiment, they constructed a microcell based on a highly-crystalline  $1\text{T}'$ -phase  $\text{MoS}_2$  NS, enabling monitoring of the activity changes step-by-step during the phase-transformed process for a fair comparison (Fig. 6i). First, keeping the contact unchanged, they showed that the basal plane  $1\text{T}'$ - $\text{MoS}_2$  (EM-1) was much more active than its 2H counterparts (EM-2), which could only be attributed to its higher intrinsic activity. Second, keeping the exposed region unchanged, they demonstrated that the  $1\text{T}'$ -metallic-phase contact (EM-2) showed a better charge-injection capability than the 2H-semiconducting- $\text{MoS}_2$  (EM-3), contributing to a high HER performance (Fig. 6j). Together, those results that were obtained by the on-chip microcells provided a unique opportunity to study the effect on electrocatalysis solely based on the crystal phase.<sup>66</sup>

## 4.2 Circuits

Besides the reaction window's function, the other one is the circuit of the on-chip microcell that stems from the FET or EDLT behavior. It provides a great platform to modulate and monitor the reaction processes with an electronic point of view, such as external electrical field modulation,<sup>67–69</sup> charge injection,<sup>59</sup> and *in situ* interface charge translation monitoring.<sup>44,70,71</sup>

**4.2.1 External electrical field modulation.** Applying the external electrical field at the interface is significantly challenging in the conventional particle-assembled electrode.<sup>72</sup> Fortunately, such modulation can be realized on an on-chip microcell due to its FET-analog circuit, capable of studying the reaction process under a back-gated electric field, as shown in Fig. 7a. Current works have demonstrated that an electric field is able to modulate the catalyst's conductivity,  $\Delta G_{\text{H}^*}$ , and the distribution of adsorbed ions.<sup>73</sup> For instance, Mai *et al.* first explored the influence of the back-gated electrical field on the conductivity of the  $\text{MoS}_2$  NS in the HER. Fig. 7b shows that applying an increased positive electric field could improve the





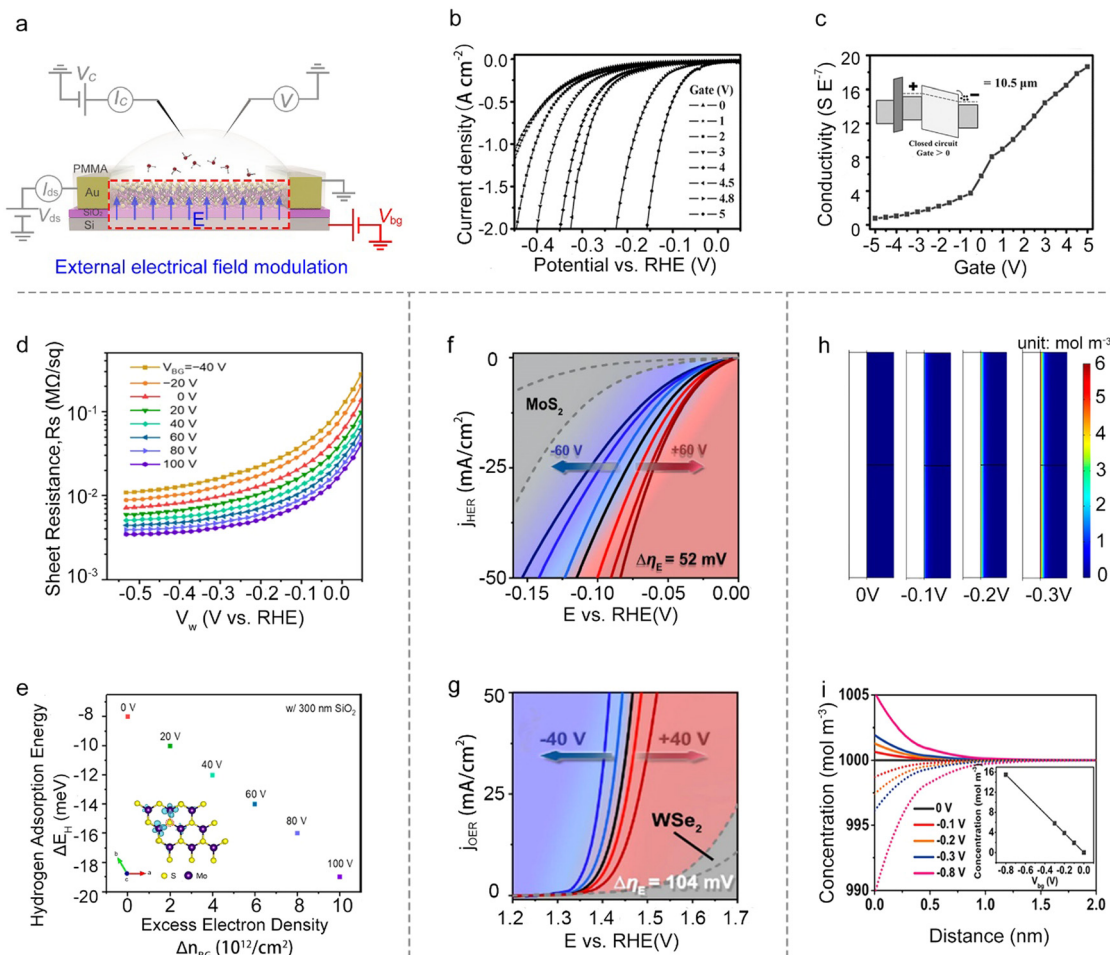


**Fig. 7** External electrical field modulation. (a) Schematic illustration of the external field electrical modulation principle via a microcell. (b) The polarization curves of the HER at different back-gate voltages. (c) The channel conductance of the MoS<sub>2</sub> NS changed with gate voltage observed in a microcell. Inset: The energy band of MoS<sub>2</sub> at the positive gate voltage bias (the inset image). (d) Sheet conductance ( $R_s$ ) at different back gate voltages ( $V_{BG}$ ) in 0.5 M H<sub>2</sub>SO<sub>4</sub> (the source-to-drain bias is 5 mV). (e) Computed hydrogen adsorption energies ( $\Delta E_{H^*}$ ) as a function of excess electron density ( $\Delta n_{BG}$ ). Inset: The charge-density map of monolayer MoS<sub>2</sub> with 5.5% S vacancies at a  $V_{BG}$  of +100 V. (f) The HER polarization curves of Pt SAs/MoS<sub>2</sub> at different back gate voltages. (g) The OER polarization curves of Co SAs/WSe<sub>2</sub> at different back gate voltages. (h) The simulation of the stationary state of net charge distribution in the interface of the electrolyte and catalyst induced by additional bias. (i) Redistribution of H<sup>+</sup> (line), SO<sub>4</sub><sup>2-</sup> (dots), and net charge (inset) induced by different back gate voltages.

HER performance; for example, the overpotential of MoS<sub>2</sub> decreased from 240 mV to 38 mV at a current density of 100 mA cm<sup>-2</sup> under 5 V gate voltage. They attributed such an improvement to the increased channel conductance of the MoS<sub>2</sub> NS, *i.e.*, from 0.0073 to 0.1776 S m<sup>-1</sup> under the gate voltage varied from -5 V to 5 V (Fig. 7c). This is further explained by the fact that the Fermi level moves closer to the bottom of the conduction band under a positive gate voltage, greatly reducing the energy barrier and thus increasing the conductivity (inset of Fig. 7c).<sup>74</sup> What is more, similar phenomena have also been observed in other works,<sup>75-77</sup> further confirming such a conductivity-modulated behavior caused by the electric field in electrocatalysis.

Besides, the electric field can also modulate  $\Delta G_{H^*}$ . For example, Frisbie *et al.* demonstrated an enhanced HER performance when increasing the back-gate voltages from -40 V to 100 V on MoS<sub>2</sub> devices. Notably, they didn't observe an

evident decrease in the sheet resistance of the monolayer MoS<sub>2</sub>, thus excluding the possible influence raised from the conductivity discussed above. Furthermore, their density functional theory (DFT) calculations showed that the gate-induced charging of the localized Mo d-states at the active (S-vacancy) sites would increase the Mo-H binding energy. Combined with theory and experiments, they claimed that the increase in HER activity is due to the increased intrinsic reactivity of the active sites in monolayer MoS<sub>2</sub> under a positive gate voltage.<sup>78</sup> A similar phenomenon was observed by other researchers.<sup>79,80</sup> Dong *et al.* demonstrated that the  $\Delta G_{H^*}$  of electron-dominated WSe<sub>2</sub> is much lower than that of hole-dominated WSe<sub>2</sub> under the electrical field modulation. Furthermore, Zhai *et al.* revealed the fact that the external field finely modulated the intermolecular charge transfer of the cobalt phthalocyanine (CoPc)/MoS<sub>2</sub> heterojunction and enhanced the Mo-H bonding.



Moreover, turning attention to the single-atom catalysts (SACs), Ding *et al.* reported the manipulation of local catalytic sites of single-atom catalysts anchored on 2D atomic crystals *via* a precisely controlled external electric field. Using the microcell, a series of model SACs have been systematically studied, such as Pt single atoms (SAs) and Co SAs on n-type MoS<sub>2</sub>, p-type WSe<sub>2</sub>, and metallic graphene. Specifically, the Pt SAs on n-type MoS<sub>2</sub> demonstrate significant improvement in HER activity under positive external electric fields (Fig. 7g), and the Co SAs on p-type WSe<sub>2</sub> achieved a dramatically-enhanced activity for the oxygen evolution reaction (OER) under negative ones (Fig. 7f). Combined with theoretical calculations, they attributed such electric field-induced performance enhancement to “onsite electrostatic polarization” in their SAC systems, where the electric field markedly influences the charge redistribution of SACs, leading to the optimization of the chemical bonding between SA and key adsorbates, the spatial distribution of outward charges, and the reaction kinetics of the rate determining steps as well.<sup>81</sup>

The external electrical field can also tune the distribution of the ions at the electrolyte-catalyst interface. For example, Mai *et al.* used the pristine VSe<sub>2</sub> NS as the catalyst and studied the distribution of the ions at the electrolyte-VSe<sub>2</sub> NS interface under varied back gate voltages. Using COMSOL simulation, they demonstrated that the back gate voltage would induce the redistribution of the ions at the interface (Fig. 7h); that is, the H<sup>+</sup> preferred to concentrate on the surface (Fig. 7i). Such a redistribution would realize the enhanced electron transport process, and thus facilitate the rate-limiting step under the HER process. As a result, they achieved a low onset

overpotential at 10 mA cm<sup>-2</sup> ( $\eta_{10} = 70$  mV) in VSe<sub>2</sub> NSs without any chemical treatment.<sup>82</sup> Overall, the external field effect is a powerful strategy to regulate the catalytic reactions; however, the above factors (*e.g.*, conductivity, intrinsic activity, and ion redistribution) would usually interfere with each other, complicating the mechanism analysis for a given reaction.

**4.2.2 Contact engineering for charge injection.** The charge injection from the substrates (or the current collector) to the catalyst is also an important factor, as shown in Fig. 8a. Distinct from the metallic one, semiconductor-type catalysts usually suffer a considerable contact resistance, which is determined by the Schottky barrier (the energy difference between the valence (or conduction) band edge of the semiconductor and the Fermi energy of the metal<sup>83</sup>) as well as the Fermi pinning effect.<sup>84</sup> Several strategies have been developed to reduce such resistance, such as heterostructures and phase engineering,<sup>20</sup> to improve the charge injection.

In heterostructures, graphene with high conductivity<sup>85</sup> and an atomically-flat behavior,<sup>86</sup> is a promising substrate to facilitate charge injection into the semiconductor materials. Such a strategy has already been widely adopted in TMD-based semiconductor devices.<sup>87,88</sup> For example, Cha *et al.* showed that the HER activity of MoS<sub>2</sub> could be improved by introducing a graphene-supporting layer to form a MoS<sub>2</sub>/graphene heterostructure.<sup>59</sup> Similarly, Chen *et al.* used a stitching contact process to directly grow the bifunctional Cr-doped WSe<sub>2</sub>/graphene for overall water splitting, as shown in Fig. 8b. They constructed a microcell based on such a heterostructure for overall water splitting (the inset of Fig. 8c), and it shows a much-lowered overpotential (a reduction of 980 mV at 10 mA cm<sup>-2</sup>)

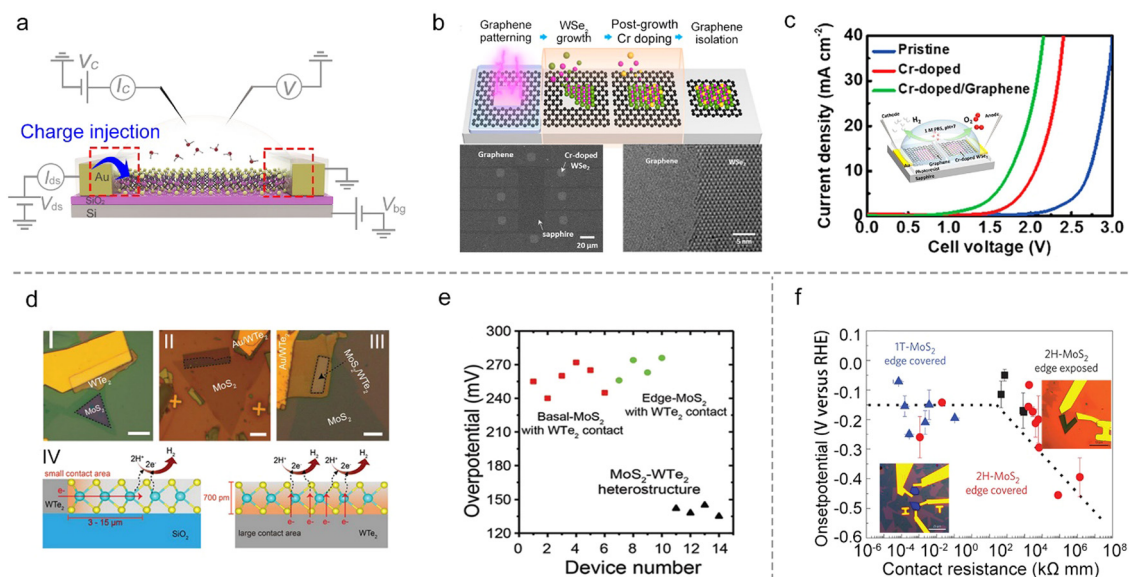


**Fig. 8** Contact engineering for charge injection. (a) Schematic illustration of the charge injection principle *via* a microcell. (b) Schematic of the formation process of the Cr-WSe<sub>2</sub>/graphene heterojunction. (c) Polarization curves of the overall water splitting of Cr-WSe<sub>2</sub>/graphene and the corresponding microcell shown in the inset image. (d) Optical images of three types of WTe<sub>2</sub>-MoS<sub>2</sub> heterostructures with WTe<sub>2</sub> contact (I, II, and III) and the charge injection pathways of WTe<sub>2</sub> edge-contact and heterostructure-contact. (e) The corresponding overpotentials of three types of heterostructures in (d). (f) The influence of the contact resistance on the HER onset potential of MoS<sub>2</sub>. Inset: The optical images of single-layer MoS<sub>2</sub> microcells with exposure of the edge (left) and the basal plane (right).



under neutral conditions as compared to that of the pristine  $\text{WSe}_2$  microcell with gold metal contact. The authors attributed such a superior performance to the self-stitching heterojunction with a lower contact resistance.<sup>89</sup> Besides the above graphene contact, Cha *et al.* also constructed a  $\text{WTe}_2$ - $\text{MoS}_2$  microcell with a  $\text{WTe}_2$  metallic contact. As shown in Fig. 8d, they systematically investigated the basal plane (I) and the edge (II) in single-layer  $\text{MoS}_2$  and the basal plane in the  $\text{MoS}_2$ - $\text{WTe}_2$  heterostructure (III) using the microcells. It turns out that type III obtained the most outstanding property with the lowest overpotential ( $135 \text{ mV} \pm 5 \text{ mV}$ ) compared to the other two types ( $255 \text{ mV} \pm 15 \text{ mV}$ ), as shown in Fig. 8e. The authors attributed such an enhancement of HER activity to the increased contact area that enhanced the charge injection to the catalyst site in the  $\text{MoS}_2$ - $\text{WTe}_2$  heterostructure (Fig. 8d IV).<sup>90</sup>

Besides the heterostructure, phase transition engineering has been used to lower the contact resistance to enhance the charge injection.<sup>91</sup> For example, Chowalla *et al.* first used phase transition engineering to provide insights into the role of electronic coupling between the substrate and  $\text{MoS}_2$  NS.<sup>20</sup> In that work, the authors made the microcells based on monolayer  $\text{MoS}_2$ , and used *n*-butyllithium to convert the 2H-phase contact into a metallic 1T-phase one (that is, phase-engineered contact). The HER catalytic properties of the basal and edge plane of  $\text{MoS}_2$  were examined, respectively, as shown in Fig. 8f. They demonstrated that phase-engineered low-resistance contact facilitated the charge injection from the substrate to the catalysts, making the activity of the 2H basal

plane (having S vacancies) comparable with 1T-phase and edge-exposed microcells (Fig. 8f). As a result, the authors claimed that the contact resistance is an essential factor, which must be evaluated when comparing the relative activities among different types of  $\text{MoS}_2$  catalysts for the HER.

**4.2.3 In situ conductance measurement.** Following the above injection process, the charges must transport to the interface before the reaction happens, and such a charge transport is usually susceptible to ion adsorption/desorption behavior, that is, EDL-modulating the channel conductance.<sup>92</sup> Thanks to the FET-analog structure, the on-chip microcell could be widely used to *in situ* study catalysts' electronic properties during the reaction process. This section introduced *in situ* charge transport measurements at semiconducting and metallic catalysts and discussed their different interfacial phenomena.

**Semiconducting catalysts.** As discussed in Section 2, an EDL-induced giant capacitance exists at the interface, which could achieve an ultrahigh carrier accumulation ( $10^{15} \text{ cm}^{-2}$  at just several volts). Such a characteristic will lead to an effective conductance modulation for semiconducting catalysts, as shown in Fig. 9a. Fortunately, the on-chip microcell allows one to *in situ* observe this conductance modulation and analyze the corresponding mechanism. For example, our group observed that the electrocatalytic reaction itself could strongly modulate the surface conductance of semiconductor electrocatalysts, and such a phenomenon was defined as self-gating.

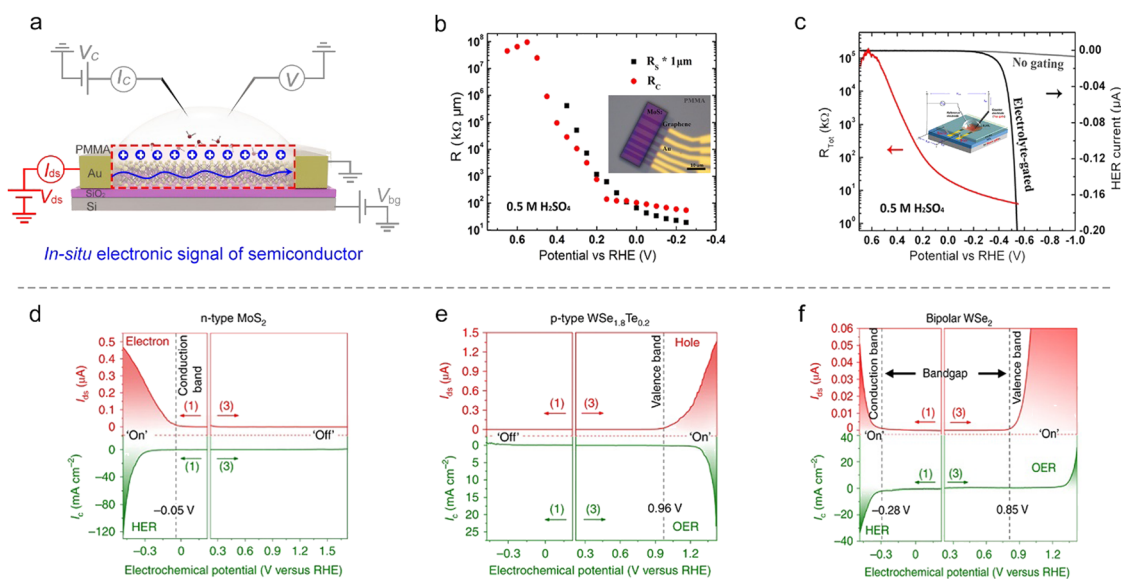


**Fig. 9** *In situ* conductance measurement on semiconductor NSs. (a) Schematic illustration of the microcell-based *in situ* electronic/electrochemical measurement. (b) The  $\text{MoS}_2$  sheet conductance ( $R_s$ ) and  $\text{MoS}_2$ /graphene device contact resistance ( $R_c$ ) recorded at different applied potentials, obtained from transfer length method (TLM) measurements. Inset: The top view of the image of the TLM platform based on a rectangle-patterned monolayer  $\text{MoS}_2$  with a graphene bottom-contact. (c) Real-time total resistance ( $R_{\text{tot}}$ ) curve (red) recorded along with the HER LSV curve (black) in 0.5 M  $\text{H}_2\text{SO}_4$ . Inset: The device with a channel length of  $1 \mu\text{m}$ . The LSV measurement was carried out at 20 mV. The gray curve shows a simulated *iR*-uncorrected HER LSV, which is extracted from the measured data (the black curve). (d)–(f) Demonstration of the self-gating phenomenon by *in situ* electronic/electrochemical measurement on n-type  $\text{MoS}_2$  (d), p-type  $\text{WSe}_{1.8}\text{Te}_{0.2}$  (e), and bipolar  $\text{WSe}_2$  (f). In (d), n-type  $\text{MoS}_2$  is turned on at a negative electrochemical potential and delivers the HER. In (e), p-type  $\text{WSe}_{1.8}\text{Te}_{0.2}$  is turned on at a positive electrochemical potential and delivers the OER. In (f), bipolar  $\text{WSe}_2$  is turned on at both negative and positive electrochemical potentials and can deliver the HER and OER.



Fig. 9d–f shows the typical *in situ* electronic/electrochemical measurements of n-type, p-type, and bipolar semiconductors during electrocatalysis, respectively. The semiconducting catalysts can be modulated to be highly conductive (“on”) or insulating (“off”), strongly correlating with the electrocatalytic reactions, that is, n-type semiconductor catalysts (e.g.,  $\text{MX}_2$ ;  $\text{M} = \text{Mo}, \text{W}, \text{Re}$ ;  $\text{X} = \text{S}, \text{Se}$ ) favor cathodic reactions such as the HER, p-type ones (e.g., Ni and Co-based catalysts) prefer anodic reactions such as the OER, and bipolar ones (e.g., Ta/Nb-doped  $\text{MoS}_2$  or  $\text{WS}_2$ ) tend to perform both anodic and cathodic reactions.<sup>93</sup>

Close to the time of the above work, Esposito *et al.* observed a similar phenomenon. In combination with the transfer length method (TLM) and microcell, they first investigated the  $\text{MoS}_2$  sheet resistance in the electrochemical environment. They found that both its sheet resistance ( $R_s$ ) and contact resistance ( $R_c$ ) decreased with the applied potential (Fig. 9b). To correlate with the HER process, they next *in situ* recorded the polarization current and the total resistance ( $R_{\text{tot}}$ ) of  $\text{MoS}_2$  simultaneously at varied HER potentials. They observed a significant decrease (up to 5 orders of magnitude) of the  $R_s$  with the HER potential, thus demonstrating a similar gating phenomenon (Fig. 9c). The authors also demonstrated that the gating efficiency is strongly dependent on the electrode configuration, where the  $\text{MoS}_2$  layer was positioned between the electrolyte and the back contact can realize the full benefits of such a gating effect.<sup>94</sup>

**Metallic catalysts.** The conductance of metallic nanostructures would also be affected under EDL, because the surface-bound

molecules would scatter their electron density.<sup>71</sup> Such an effect will be magnified as the size of nanostructures is reduced to several nanometers, e.g., ultrafine metallic NWs. Therefore, *in situ* monitoring of the metallic nanostructures’ conductance also presents a potential method to study ion adsorption/desorption behavior during the reaction process, as shown in Fig. 10a.

The first example is that Ding *et al.* developed a microcell to directly probe the electrochemical interfaces of Pt NWs.<sup>95</sup> They showed that the electrical properties of ultrafine Pt NWs are susceptible and selective to the electrochemical surface states. The redox regions, e.g., HER, H adsorption/desorption region ( $\text{H}_{\text{upd}}$ ), double layer (DL) region, surface oxide formation/reduction region ( $\text{O}_{\text{upd}}$ ), and OER could be clearly distinguished from  $I_G$ – $V_G$  and normalized  $G_{\text{SD}}$ – $V_G$  curves, as shown in Fig. 10b. Using the microcell-based *in situ* measurement, they also examined a series of electrocatalytic reactions such as the  $\text{H}_2\text{O}_2$  reduction and oxidation reactions, methanol oxidation reaction (MOR), and formic acid oxidation reaction (FOR), demonstrating the reliability and generality of this method.

Focusing on the influence of electrolytes on the HER, Duan *et al.* elaborated on the fundamental role of different cations ( $\text{Li}^+$ ,  $\text{Na}^+$ , and  $\text{K}^+$ ) in HER kinetics using *in situ* charge transport measurement (Fig. 10c). By combining systematic experiments and theoretical studies, they concluded that the surface coverage of  $\text{OH}_{\text{ad}}$  was enhanced by the presence of small cations ( $\text{Li}^+$ ),<sup>25</sup> as shown in Fig. 10c. Interestingly, such a method can be extendable to more complex electrochemical reactions such as the  $\text{CO}_2$  reduction reaction ( $\text{CO}_2\text{RR}$ ). For example, Ding *et al.*

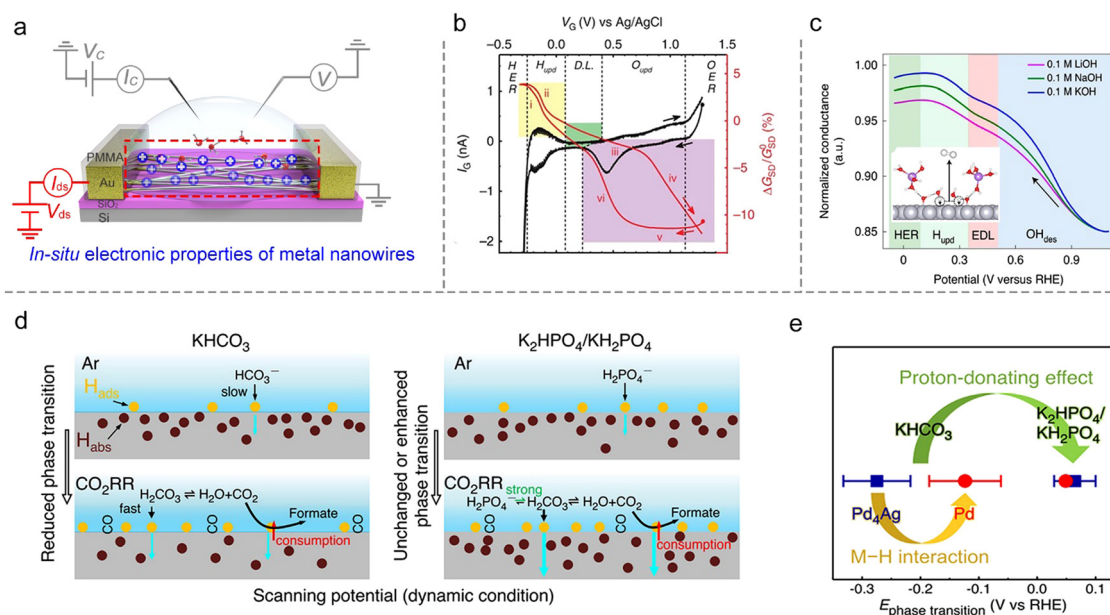


**Fig. 10** *In situ* conductance measurement on metal NWs. (a) Schematic illustration of the microcell-based *in situ* electronic/electrochemical measurement on metal NWs. (b)  $I_G$ – $V_G$  curves (in black) and normalized  $G_{\text{SD}}$  (conductance)– $V_G$  curves (in red) of a typical Pt NW microcell. (c) Normalized *in situ* conductance signal recorded at different potentials of the Pt NW device in 0.1 M MOH ( $\text{M} = \text{Li}, \text{Na}, \text{and K}$ ) electrolyte. Inset: The  $\text{Li}^+$  enhances the coverage of  $\text{OH}_{\text{ad}}$ . (d) Schematic illustration of different Pd–H states at the interfaces in  $\text{KHCO}_3$  (left panel) and  $\text{K}_2\text{HPO}_4/\text{KH}_2\text{PO}_4$  (right panel) during the  $\text{CO}_2\text{RR}$  processes. The yellow and brown cycles represent the adsorbed H on the surface ( $\text{H}_{\text{ads}}$ ) and absorbed H in the bulk ( $\text{H}_{\text{abs}}$ ), respectively. (e) Summary of phase transition potentials of Pd (red) and  $\text{Pd}_4\text{Ag}$  (blue) under  $\text{CO}_2\text{RR}$  conditions in  $\text{KHCO}_3$  and  $\text{K}_2\text{HPO}_4/\text{KH}_2\text{PO}_4$  obtained at  $10 \text{ mV s}^{-1}$ .





**Table 1** Strategies of optimizing the catalyst design and exploring electrochemical interfacial phenomena

| Strategies                      | Types   | Materials  | Performances  | Electrolyte   | Ref.     |
|---------------------------------|---|--|---|---|----------|
| Identification                  | Phases<br>GBs   | 1T'-MoS <sub>2</sub>   | HER: $\eta_{\text{onset}}$ : 205 mV; Tafel slope: 51 mV dec <sup>-1</sup>   | 0.5 M H <sub>2</sub> SO <sub>4</sub>  | 57       |
|                                 |   | MoS <sub>2</sub> nanograin film  | HER: $\eta_{10}$ : 25 mV; Tafel slope: 54 mV dec <sup>-1</sup>  | 0.5 M H <sub>2</sub> SO <sub>4</sub>  | 48       |
| Monitoring                      | Edges   | 2H-1T'-MoS <sub>2</sub> GBs  | HER: $\eta_{\text{onset}}$ : 260 mV; Tafel slope: 85 mV dec <sup>-1</sup>   | 0.5 M H <sub>2</sub> SO <sub>4</sub>  | 58       |
|                                 |   | MoTe <sub>2</sub> films  | HER: $\eta_{\text{onset}}$ : 211 mV; Tafel slope: 98 mV dec <sup>-1</sup>   | 0.5 M H <sub>2</sub> SO <sub>4</sub>  | 49       |
|                                 |   | 1T'-MoS <sub>2</sub>   | HER: $\eta_{\text{onset}}$ : 77 mV; Tafel slope: 56 mV dec <sup>-1</sup>  | 0.5 M H <sub>2</sub> SO <sub>4</sub>  | 50       |
|                                 |   | WTe <sub>2</sub> flakes  | HER: $\eta_{\text{onset}}$ : 320 mV; Tafel slope: 110 mV dec <sup>-1</sup>  | 0.5 M H <sub>2</sub> SO <sub>4</sub>  | 59       |
|                                 |   | P-MoS <sub>2</sub>   | HER: $\eta_{10}$ : 297 mV; Tafel slope: 97 mV dec <sup>-1</sup>   | 0.5 M H <sub>2</sub> SO <sub>4</sub>  | 54       |
|                                 |   | Mo-MoS <sub>2</sub>  | HER: $\eta_{\text{onset}}$ : 107 mV; Tafel slope: 36.4 mV dec <sup>-1</sup>   | 0.5 M H <sub>2</sub> SO <sub>4</sub>  | 64       |
| Monitoring                      | Amorphization<br>Defect engineering<br>Thickness        | PSe <sub>x</sub> NSs   | HER: smaller onset overpotential and Tafel slope with a treatment duration from 0 to 60 s   | 0.5 M H <sub>2</sub> SO <sub>4</sub>  | 10       |
|                                 |   | MoTe <sub>2</sub> NSs  | HER: smaller onset overpotential and Tafel slope with an increase in the degree of oxidation  | 0.5 M H <sub>2</sub> SO <sub>4</sub>  | 65       |
|                                 |   | Individual PtSe <sub>2</sub> flakes  | HER: smaller overpotential and Tafel slope with increasing layer numbers  | 0.5 M H <sub>2</sub> SO <sub>4</sub>  | 51       |
|                                 |   | 1T'-MoS <sub>2</sub>   | HER: $\eta_{\text{onset}}$ : 65 mV; Tafel slope: 100 mV dec <sup>-1</sup>   | 0.5 M H <sub>2</sub> SO <sub>4</sub>  | 66       |
| External field regulation       | Improve conductivity<br>Activate the intrinsic activity | MoS <sub>2</sub>   | HER: back-gate voltage 5 V, $\eta_{100}$ : 38 mV; Tafel slope: 110 mV dec <sup>-1</sup>   | 0.5 M H <sub>2</sub> SO <sub>4</sub>  | 75       |
|                                 |   | MoS <sub>2</sub>   | Back-gate voltage -40 V, $\eta_{50}$ : 524 ± 8 mV; Tafel slope: 164 ± 1 mV dec <sup>-1</sup>  | 0.5 M H <sub>2</sub> SO <sub>4</sub>  | 79       |
| Charge injection                | Heterostructure   | WSe <sub>2</sub>   | Back-gate voltage 100V, $\eta_{50}$ : 334 ± 3 mV; Tafel slope: 100 ± 6 mV dec <sup>-1</sup>   | 0.5 M H <sub>2</sub> SO <sub>4</sub>  | 80       |
|                                 |   | CoPc/MoS <sub>2</sub>  | HER: back-gate voltage 5 V, $\eta_{10}$ : 280 mV; Tafel slope: 104 mV dec <sup>-1</sup>   | 0.5 M H <sub>2</sub> SO <sub>4</sub>  | 81       |
|                                 |   | Pt SAs/MoS <sub>2</sub>  | HER: back-gate voltage 2V, $\eta_{10}$ : 238 mV; Tafel slope: 115 mV dec <sup>-1</sup>  | 0.5 M H <sub>2</sub> SO <sub>4</sub>  | 82       |
|                                 |   | Co SAs/WSe <sub>2</sub>  | HER: back-gate voltage from +60 V to -60 V, $\Delta\eta_{50}$ : 52 mV; Tafel slope: from 117 mV dec <sup>-1</sup> to 65 mV dec <sup>-1</sup>  | 0.1 M KOH   |          |
|                                 |   | VSe <sub>2</sub>   | OER: back-gate voltage from +40 V to -40 V, $\Delta\eta_{50}$ : 104 mV; Tafel slope: from 281 mV dec <sup>-1</sup> to 64 mV dec <sup>-1</sup>   | 0.5 M H <sub>2</sub> SO <sub>4</sub>  | 83       |
|                                 |   | MoS <sub>2</sub> /graphene   | HER: bate-gate voltage (0 V), $\eta_{10}$ : 126 mV; Tafel slope: 70 mV dec <sup>-1</sup>  | 0.5 M H <sub>2</sub> SO <sub>4</sub>  | 60       |
|                                 |   | Cr-doped WSe <sub>2</sub> /graphene  | Bate-gate voltage (-1 V), $\eta_{10}$ : 70 mV; Tafel slope: 55 mV dec <sup>-1</sup>   | 0.5 M H <sub>2</sub> SO <sub>4</sub>  | 90       |
|                                 |   | MoS <sub>2</sub> /WTe <sub>2</sub>   | HER: MoS <sub>2</sub> /graphene shows better performance than MoS <sub>2</sub> with graphene contact  | 1 M PBS   |          |
|                                 |   | MoS <sub>2</sub> contact   | Overall water splitting: with a 310 mV reduction in cell voltage at 10 mA cm <sup>-2</sup> compared to the Cr-doped WSe <sub>2</sub> microcells with the gold contact   | 0.5 M H <sub>2</sub> SO <sub>4</sub>  | 91       |
|                                 |   | MoS <sub>2</sub> , WSe <sub>2</sub> , Te <sub>0.2</sub> and WSe <sub>2</sub> | HER: MoS <sub>2</sub> -WTe <sub>2</sub> heterostructure shows the lowest overpotentials (-135 ± 5 mV)   | 0.5 M H <sub>2</sub> SO <sub>4</sub>  | 20       |
| In situ conductance measurement | Metallic catalyst                                       | Pt NWs   | HER: basal plane of 2H MoS <sub>2</sub> with low contact resistance is comparable to that of 1T phase and edge of 2H phase  | 0.5 M H <sub>2</sub> SO <sub>4</sub>  | 94       |
|                                 |   | Pt NWs   | The type of semiconductor catalysts strongly correlate with their electrocatalysis  | 0.5 M H <sub>2</sub> SO <sub>4</sub>  | 95       |
|                                 |   | Pd NWs and Pd <sub>4</sub> Ag NWs  | HER: electrolyte gating lowering the contact resistance<br>Providing a new strategy to <i>in situ</i> monitor the electrochemical surface conditions of metal nanocatalysts<br>Smaller cations favor a high OH <sub>ad</sub> coverage on the Pt surface in the HER potential window | 0.5 M H <sub>2</sub> SO <sub>4</sub><br>0.5 M H <sub>2</sub> SO <sub>4</sub>                                    | 96       |
|                                 |   |  | The proton-donating capacity of near neutral electrolytes serve as a key impacting factor to H sorption kinetics and CO <sub>2</sub> RR   | 0.1 M KOH LiOH or NaOH<br>KHCO <sub>3</sub> or K <sub>2</sub> HPO <sub>4</sub> /KH <sub>2</sub> PO <sub>4</sub> | 25<br>97 |

utilized microcells to monitor and quantify the H sorption process on different metallic NWs (Pd, Pt, Au, Pd<sub>4</sub>Ag) during the CO<sub>2</sub>RR process. The authors revealed a competitive relationship between electrochemical CO<sub>2</sub>RR and hydrogen sorption kinetics, related to the local electrolyte environment (proton donors with different pK<sub>a</sub>), as shown in Fig. 10d. Moreover, a more negative phase transition potential was also observed in Pd<sub>4</sub>Ag, giving direct evidence for the weakened M–H interaction in alloy catalysts to promote the CO<sub>2</sub>RR (Fig. 10e).<sup>96</sup>

## 5. Conclusion

The electrocatalytic strategies have attracted increasing research interest in developing clean and sustainable energy. However, the common particle-assembled measurement has faced several limitations, such as average results of thousands of samples, complex reaction interface, and unclear charge-flowing pathway in the electrodes. With the maturation of micro-nano processing technology, the on-chip microcell that

provides an effective means to study the catalytic properties at a single NW/NS level, has shown growing potential in electrocatalysis. Table 1 highlights the current achievements based on on-chip electrocatalytic microcells. For example, making use of the reaction window, the on-chip microcell enables the identification of the active site or monitoring of its changes at a single nanomaterial level, such as (i) identification of the HER activity of GBs, edges, different phases and doping, and heterostructures, as well as (ii) monitoring of the phase transition, GB changes, and defect engineering. On the other hand, taking advantage of the circuits, many fantastic strategies can be developed to shed insight into the reaction behaviors, such as external electrical field modulation, contact engineering for charge injection, and *in situ* conductance measurements as well.

Although significant progress has been made on on-chip electrocatalytic microcells over the last decade, its research is still in its infancy. There would be a long way to explore its true potential. Hence, we propose our prospects in this emerging field, as illustrated in Fig. 11.

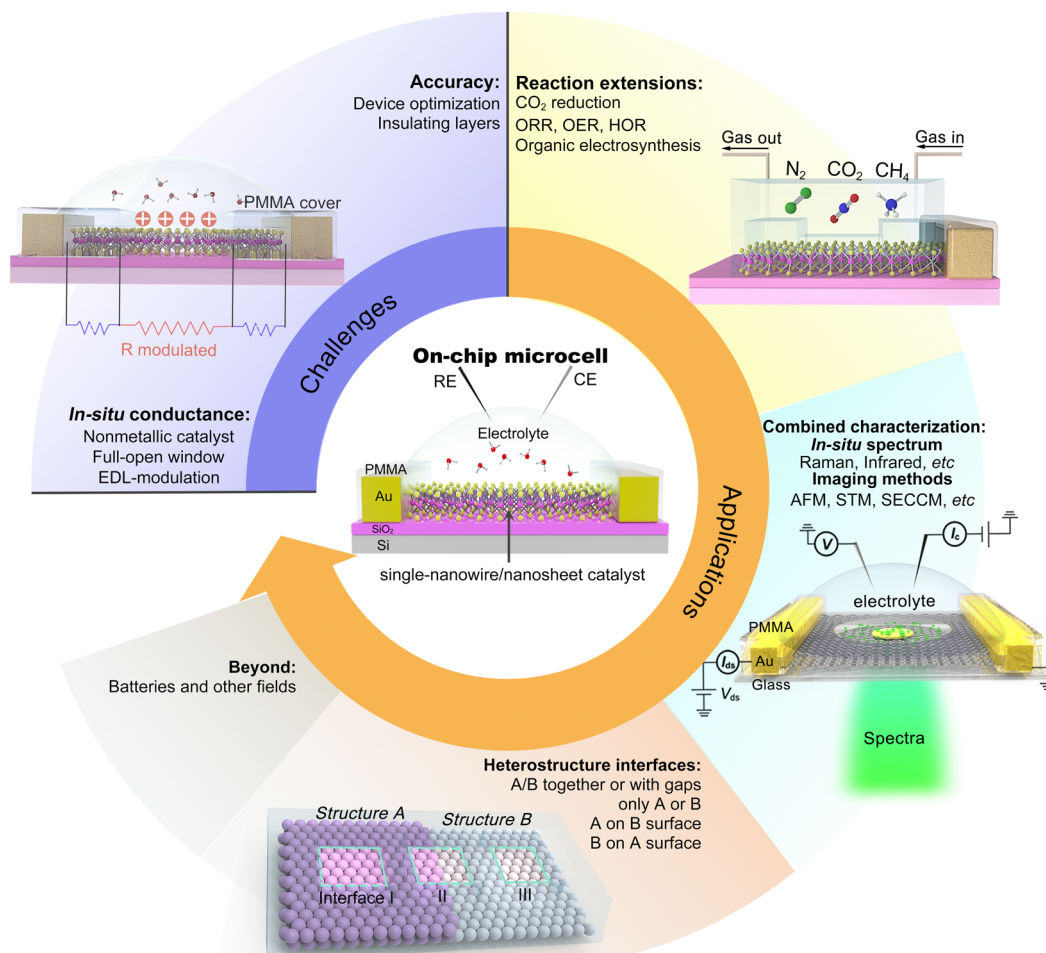


**Fig. 11** Prospects for on-chip microcells. The challenges in this emergent field, such as measurement accuracy and the conductance issue, are discussed. The applications of the on-chip microcells, e.g., the generality (reaction extension), guidance (model catalysis), multi-functions (combined strategy), and others, are also expected.



## 5.1 Challenges

**5.1.1 Measurement accuracy.** The current size of the reaction window is usually  $> 1 \mu\text{m}^2$ . As is well-known, small size is highly desirable for on-chip electrocatalytic microcells to achieve a high spatial resolution. Unfortunately, a smaller window leads to a weaker signal collected, making the measurements highly susceptible to external factors such as working conditions and noise of electrical lines. For example, when the order of microcell signals is about  $10^{-9}$  A, an accurate evaluation of the Tafel slope extracted in the HER polarization curve will require the background noise current to be as low as  $10^{-11}$  A (nearly close to the limit of the source meter). Therefore, how to decrease the window size while eliminating possible signal interfaces is still challenging. Here, optimization of the device structure, development of the SMU circuit, and exploration of other insulating layers (*e.g.*, amorphous  $\text{SiO}_x$  or  $\text{AlO}_x$  layer) are suggested.

**5.1.2 Conductance issue.** As mentioned above, the on-chip electrocatalytic microcell, essentially, is based on the structure of the electronic device; as a result, good conductivity is a premise, especially for nonmetallic catalysts. Recent work has demonstrated that the EDL had a strong modulation on the conductivity of  $> 30$  types of nonmetallic catalysts (self-gating phenomenon), covering a series of reactions such as the HER,  $\text{CO}_2\text{RR}$ , OER, and oxygen reduction reaction (ORR). It should be noted that such an EDL-modulation can make nonmetallic catalysts highly conductive or insulating, indeed being a critical factor in affecting the charge transport. Therefore, the *in situ* examination of the channel conductance is needed when we collect the electrochemical reaction current in a microcell, strictly promising the reliability of the measured data. On the other hand, during the fabrication process, the reaction window may not fully expose the catalyst channel, thus failing to tune the whole device to be conductive. Therefore, paying much attention to the window position carved on the insulating layer is also necessary.

## 5.2 Applications

**5.2.1 Reaction extension.** The current research mainly focuses on the HER, OER, or ORR in an aqueous electrolyte. Extending it to other complicated electrocatalytic systems, such as the  $\text{CO}_2\text{RR}$ ,  $\text{N}_2$  reduction reaction ( $\text{N}_2\text{RR}$ ),  $\text{CH}_4$  oxidation reaction ( $\text{CH}_4\text{OR}$ ), and electrocatalytic conversion of small organic molecules, is meaningful towards the generality of on-chip microcells. However, the encountered limitation is that gas and liquid products are too little to be collected and quantified, making it challenging to determine complex intermediates, Faraday's efficiency, and the conversion. Therefore, combining microfluidic flow cells and in-line product analysis with microcells shows potential for other complicated electrocatalytic systems.

**5.2.2 Model catalysis.** The model-catalysis research provides great potential to shed light on the principle of the classic catalytic reactions. Benefiting from the micro-nano processing technology, the on-chip microcell enables the construction of a

clear model catalytic interface, such as heterostructure catalysis with defined interfaces or components. Herein, taking the alkaline HER as an example, heterostructure catalysts with two components (*i.e.*, one is for water dissociation, and the other is for hydrogen formation steps) are usually designed, while the catalytic mechanisms are still in debate; for example, clarifying how they interact between each other (hydrogen diffusion from one to the other) or distinguishing which reaction pathways dominate. Fortunately, using an on-chip microcell, an ideal model two-component interface like A/B together or with gaps, only A or B, A on B surface or B on A surface, can be constructed through the micro-nano processing technology, and their detailed catalytic properties can be examined through reaction windows. Moreover, taking advantage of a recently-developed sub-10 nm processing technology, insights into their interaction down to a molecular or atomic level will be achievable in the future.

**5.2.3 Combined strategy.** The data provided by the current on-chip microcell is only based on the reaction current and/or conductance current. To give a full picture of the whole reaction process (*e.g.*, morphology/structure evolution, ion adsorption/desorption, or the kinetic process), a combination of spectrographic and/or imaging characterization techniques is encouraged, such as *in situ* XRD, XPS, TEM, TIRF (total internal reflection fluorescence microscopy), Raman, IR, *etc.*<sup>97-102</sup> For example, combined with Raman and IR, the structure change of the catalyst and the reaction intermediates would be detectable during the reaction process. Alternatively, using TIRF technology, nanobubbles can be labeled by single fluorophores, allowing us to reveal the process of gas nucleation to desorption and their detailed three-phase interfacial dynamics.<sup>103</sup> On the microcell side, integrating a working electrode, counter electrode, and reference electrode on a chip is needed, making such a combination strategy more feasible.

**5.2.4 Beyond.** Besides electrocatalysis, on-chip microcell research can also be used in other electrochemical processes like batteries. For instance, Mai *et al.* designed and assembled an all-solid-state single nanowire battery for *in situ* detecting the charge and discharge processes.<sup>18</sup> Parkin *et al.* realized the epitaxial growth of single-crystalline  $\text{T-Nb}_2\text{O}_5$  thin films with vertical 2D channels, showing a larger and faster resistance change and a wider voltage operation range during Li interaction.<sup>104</sup> Besides, Cui *et al.* first reported the *in situ* study of the electrochemical generation of sulfur on 2D layered materials, and correlated the varied sulfur states with the corresponding electrochemical behaviors, which shed light on the electrode design for high-performance Li-S batteries.<sup>105</sup>

The on-chip microcell can be expandable to other fields, such as photovoltaics, photoelectrochemical, thermoelectric, and electroanalysis. For example, in photovoltaics, as early as 2007, Lieber *et al.* reported an on-chip single p-i-n silicon nanowire solar cell.<sup>106</sup> In photoelectrochemistry, Geim *et al.* reported a strong dependence of the photoelectrochemical properties on the number of  $\text{MoS}_2$  layers with the help of an on-chip platform.<sup>107</sup> In thermoelectrics, Zeng *et al.* investigated the thermoelectric transport of 2D indium selenide ( $\text{InSe}$ ) with



different thicknesses under the gate voltages.<sup>108</sup> In electrodiagnosis, Geim *et al.* investigated a series of monolayer crystals to explore the proton transport properties of the atomic-thick layer, promoting the development of electrodiagnosis and the utilization of blue energy.<sup>109</sup> Based on those efforts, more tantalizing applications are encouraged to be underway and come to fruition shortly.

## Conflicts of interest

The authors declare no conflict of interest.

## Acknowledgements

Y. H. acknowledges the National Key R&D Program of China (2021YFA1500900), the Fundamental Research Funds for Central Universities (531119200209), and the National Natural Science Foundation of China (52203354 and 22272048).

## References

- W. Ahmad, P. Koley, S. Dwivedi, R. Lakshman, Y. K. Shin, A. C. T. van Duin, A. Shrotri and A. Tanksale, *Nat. Commun.*, 2023, **14**, 304.
- X. Zhu, H. Zong, C. J. V. Pérez, H. Miao, W. Sun, Z. Yuan, S. Wang, G. Zeng, H. Xu, Z. Jiang and G. A. Ozin, *Angew. Chem., Int. Ed.*, 2023, **62**, e2022186.
- H. Nishiyama, T. Yamada, M. Nakabayashi, Y. Maehara, M. Yamaguchi, Y. Kuromiya, Y. Nagatsuma, H. Tokudome, S. Akiyama, T. Watanabe, R. Narushima, S. Okunaka, N. Shibata, T. Takata, T. Hisatomi and K. Domen, *Nature*, 2021, **598**, 304–307.
- P. Zhou, I. A. Navid, Y. Ma, Y. Xiao, P. Wang, Z. Ye, B. Zhou, K. Sun and Z. Mi, *Nature*, 2023, **613**, 66–70.
- T. S. Teitworth, D. J. Hill, S. R. Litvin, E. T. Ritchie, J.-S. Park, J. P. Custer, A. D. Taggart, S. R. Bottum, S. E. Morley, S. Kim, J. R. McBride, J. M. Atkin and J. F. Cahoon, *Nature*, 2023, **614**, 270–274.
- Y. Jiao, Y. Zheng, M. Jaroniec and S. Z. Qiao, *Chem. Soc. Rev.*, 2015, **44**, 2060–2086.
- M. Liu, Y. Pang, B. Zhang, P. De Luna, O. Voznyy, J. Xu, X. Zheng, C. T. Dinh, F. Fan, C. Cao, F. P. G. de Arquer, T. S. Safaei, A. Mepham, A. Klinkova, E. Kumacheva, T. Filleter, D. Sinton, S. O. Kelley and E. H. Sargent, *Nature*, 2016, **537**, 382–386.
- C. Chen, X. Zhu, X. Wen, Y. Zhou, L. Zhou, H. Li, L. Tao, Q. Li, S. Du, T. Liu, D. Yan, C. Xie, Y. Zou, Y. Wang, R. Chen, J. Huo, Y. Li, J. Cheng, H. Su, X. Zhao, W. Cheng, Q. Liu, H. Lin, J. Luo, J. Chen, M. Dong, K. Cheng, C. Li and S. Wang, *Nat. Chem.*, 2020, **12**, 717–724.
- Q. Wang, T. Li, C. Yang, M. Chen, A. Guan, L. Yang, S. Li, X. Lv, Y. Wang and G. Zheng, *Angew. Chem., Int. Ed.*, 2021, **60**, 17398–17403.
- Y. He, L. Liu, C. Zhu, S. Guo, P. Golani, B. Koo, P. Tang, Z. Zhao, M. Xu, C. Zhu, P. Yu, X. Zhou, C. Gao, X. Wang, Z. Shi, L. Zheng, J. Yang, B. Shin, J. Arbiol, H. Duan, Y. Du, M. Heggen, R. E. Dunin-Borkowski, W. Guo, Q. J. Wang, Z. Zhang and Z. Liu, *Nat. Catal.*, 2022, **5**, 212–221.
- P. Garrido-Barros, J. Derosa, M. J. Chalkley and J. C. Peters, *Nature*, 2022, **609**, 71–76.
- B. Zhu, B. Dong, F. Wang, Q. Yang, Y. He, C. Zhang, P. Jin and L. Feng, *Nat. Commun.*, 2023, **14**, 1686.
- W. Shao, M. Xiao, C. Yang, M. Cheng, S. Cao, C. He, M. Zhou, T. Ma, C. Cheng and S. Li, *Small*, 2021, **18**, 2105763.
- Y. j Wu, J. Yang, T. x Tu, W. q Li, P. f Zhang, Y. Zhou, J. f Li, J. t Li and S. G. Sun, *Angew. Chem., Int. Ed.*, 2021, **60**, 26829–26836.
- S. Song, J. Zhou, X. Su, Y. Wang, J. Li, L. Zhang, G. Xiao, C. Guan, R. Liu, S. Chen, H.-J. Lin, S. Zhang and J.-Q. Wang, *Energy Environ. Sci.*, 2018, **11**, 2945–2953.
- A. L. Strickler, M. a Escudero-Escribano and T. F. Jaramillo, *Nano Lett.*, 2017, **17**, 6040–6046.
- H. Jin, S. Choi, G. J. Bang, T. Kwon, H. S. Kim, S. J. Lee, Y. Hong, D. W. Lee, H. S. Park, H. Baik, Y. Jung, S. J. Yoo and K. Lee, *Energy Environ. Sci.*, 2022, **15**, 1119–1130.
- L. Mai, Y. Dong, L. Xu and C. Han, *Nano Lett.*, 2010, **10**, 4273–4278.
- M. Ding, Q. He, G. Wang, H.-C. Cheng, Y. Huang and X. Duan, *Nat. Commun.*, 2015, **6**, 7867.
- D. Voiry, R. Fullon, J. Yang, E. S. C. de Carvalho Castro, R. Kappera, I. Bozkurt, D. Kaplan, M. J. Lagos, P. E. Batson, G. Gupta, A. D. Mohite, L. Dong, D. Er, V. B. Shenoy, T. Asefa and M. Chhowalla, *Nat. Mater.*, 2016, **15**, 1003–1009.
- J. Qi, W. Wang, Y. Li, Y. Sun, Z. Wu, K. Bao, L. Wang, R. Ye, M. Ding and Q. He, *Small*, 2022, **18**, 2204010.
- C.-H. Kim and C. D. Frisbie, *J. Am. Chem. Soc.*, 2016, **138**, 7220–7223.
- Y. Wang, C.-H. Kim, Y. Yoo, J. E. Johns and C. D. Frisbie, *Nano Lett.*, 2017, **17**, 7586–7592.
- Y. He, Q. He, L. Wang, C. Zhu, P. Golani, A. D. Handoko, X. Yu, C. Gao, M. Ding, X. Wang, F. Liu, Q. Zeng, P. Yu, S. Guo, B. I. Yakobson, L. Wang, Z. W. Seh, Z. Zhang, M. Wu, Q. J. Wang, H. Zhang and Z. Liu, *Nat. Mater.*, 2019, **18**, 1098–1104.
- A. H. Shah, Z. Zhang, Z. Huang, S. Wang, G. Zhong, C. Wan, A. N. Alexandrova, Y. Huang and X. Duan, *Nat. Catal.*, 2022, **5**, 923–933.
- S. Najmaei, A. L. Glasmann, M. A. Schroeder, W. L. Sarney, M. L. Chin and D. M. Potrepka, *Mater. Today*, 2022, **59**, 80–106.
- J. A. del Alamo, *Nature*, 2011, **479**, 317–323.
- I. Ferain, C. A. Colinge and J.-P. Colinge, *Nature*, 2011, **479**, 310–316.
- Z. Cheng, C.-S. Pang, P. Wang, S. T. Le, Y. Wu, D. Shahrjerdi, I. Radu, M. C. Lemme, L.-M. Peng, X. Duan, Z. Chen, J. Appenzeller, S. J. Koester, E. Pop, A. D. Franklin and C. A. Richter, *Nat. Electron.*, 2022, **5**, 416–423.
- H. Du, X. Lin, Z. Xu and D. Chu, *J. Mater. Sci.*, 2015, **50**, 5641–5673.





- 31 B. Radisavljevic, A. Radenovic, J. Brivio, V. Giacometti and A. Kis, *Nat. Nanotechnol.*, 2011, **6**, 147–150.
- 32 Y. Wu, S. Ringe, C.-L. Wu, W. Chen, A. Yang, H. Chen, M. Tang, G. Zhou, H. Y. Hwang, K. Chan and Y. Cui, *Nano Lett.*, 2019, **19**, 7293–7300.
- 33 Y.-G. Ha, K. Everaerts, M. C. Hersam and T. J. Marks, *Acc. Chem. Res.*, 2014, **47**, 1019–1028.
- 34 F. Torricelli, D. Z. Adrahtas, Z. Bao, M. Berggren, F. Biscarini, A. Bonfiglio, C. A. Bortolotti, C. D. Frisbie, E. Macchia, G. G. Malliaras, I. McCulloch, M. Moser, T. Q. Nguyen, R. M. Owens, A. Salleo, A. Spanu and L. Torsi, *Nat. Rev. Methods Primers*, 2021, **1**, 66.
- 35 P. Liu, B. Lei, X. Chen, L. Wang and X. Wang, *Nat. Rev. Phys.*, 2022, **4**, 336–352.
- 36 S. Z. Bisri, S. Shimizu, M. Nakano and Y. Iwasa, *Adv. Mater.*, 2017, **29**, 1607054.
- 37 Y. J. Zhang, J. T. Ye, Y. Yomogida, T. Takenobu and Y. Iwasa, *Nano Lett.*, 2013, **13**, 3023–3028.
- 38 C. Leighton, *Nat. Mater.*, 2019, **18**, 13–18.
- 39 S. H. Kim, K. Hong, W. Xie, K. H. Lee, S. Zhang, T. P. Lodge and C. D. Frisbie, *Adv. Mater.*, 2013, **25**, 1822–1846.
- 40 M. Nakano, K. Shibuya, D. Okuyama, T. Hatano, S. Ono, M. Kawasaki, Y. Iwasa and Y. Tokura, *Nature*, 2012, **487**, 459–462.
- 41 X. Tong, Y. Zhao, Z. Zhuo, Z. Yang, S. Wang, Y. Liu, N. Lu, H. Li and T. Zhai, *Angew. Chem., Int. Ed.*, 2022, **61**, e202112953.
- 42 W. Wang, Y. Song, C. Ke, Y. Li, Y. Liu, C. Ma, Z. Wu, J. Qi, K. Bao, L. Wang, J. Wu, S. Jiang, J. Zhao, C.-S. Lee, Y. Chen, G. Luo, Q. He and R. Ye, *ACS Nano*, 2023, **17**, 1287–1297.
- 43 Z. Mu, M. Yang, W. He, Y. Pan, P. Zhang, X. Li, X. Wu and M. Ding, *J. Phys. Chem. Lett.*, 2020, **11**, 5798–5806.
- 44 B. Tian, H. Shin, S. Liu, M. Fei, Z. Mu, C. Liu, Y. Pan, Y. Sun, W. A. Goddard, 3rd and M. Ding, *Angew. Chem., Int. Ed.*, 2021, **60**, 16448–16456.
- 45 H. Xia, Z. Shi, C. Gong and Y. He, *J. Mater. Chem. A*, 2022, **10**, 19067–19089.
- 46 D. Voiry, M. Salehi, R. Silva, T. Fujita, M. Chen, T. Asefa, V. B. Shenoy, G. Eda and M. Chhowalla, *Nano Lett.*, 2013, **13**, 6222–6227.
- 47 Y. Chen, Z. Lai, X. Zhang, Z. Fan, Q. He, C. Tan and H. Zhang, *Nat. Rev. Chem.*, 2020, **4**, 243–256.
- 48 Y. He, P. Tang, Z. Hu, Q. He, C. Zhu, L. Wang, Q. Zeng, P. Golani, G. Gao, W. Fu, Z. Huang, C. Gao, J. Xia, X. Wang, X. Wang, C. Zhu, Q. M. Ramasse, A. Zhang, B. An, Y. Zhang, S. Marti-Sanchez, J. R. Morante, L. Wang, B. K. Tay, B. I. Yakobson, A. Trampert, H. Zhang, M. Wu, Q. J. Wang, J. Arbiol and Z. Liu, *Nat. Commun.*, 2020, **11**, 57.
- 49 Y. Lee, N. Ling, D. Kim, M. Zhao, Y. A. Eshete, E. Kim, S. Cho and H. Yang, *Adv. Funct. Mater.*, 2021, **32**, 2105675.
- 50 J. Zhang, J. Wu, H. Guo, W. Chen, J. Yuan, U. Martinez, G. Gupta, A. Mohite, P. M. Ajayan and J. Lou, *Adv. Mater.*, 2017, **29**, 1701955.
- 51 D. Hu, T. Zhao, X. Ping, H. Zheng, L. Xing, X. Liu, J. Zheng, L. Sun, L. Gu, C. Tao, D. Wang and L. Jiao, *Angew. Chem., Int. Ed.*, 2019, **58**, 6977–6981.
- 52 Y. Zang, S. Niu, Y. Wu, X. Zheng, J. Cai, J. Ye, Y. Xie, Y. Liu, J. Zhou, J. Zhu, X. Liu, G. Wang and Y. Qian, *Nat. Commun.*, 2019, **10**, 1217.
- 53 Z. Zheng, L. Yu, M. Gao, X. Chen, W. Zhou, C. Ma, L. Wu, J. Zhu, X. Meng, J. Hu, Y. Tu, S. Wu, J. Mao, Z. Tian and D. Deng, *Nat. Commun.*, 2020, **11**, 3315.
- 54 W. Wang, Y. Song, C. Ke, Y. Li, Y. Liu, C. Ma, Z. Wu, J. Qi, K. Bao, L. Wang, J. Wu, S. Jiang, J. Zhao, C. S. Lee, Y. Chen, G. Luo, Q. He and R. Ye, *ACS Nano*, 2023, **17**, 1287–1297.
- 55 M. A. Lukowski, A. S. Daniel, F. Meng, A. Forticaux, L. Li and S. Jin, *J. Am. Chem. Soc.*, 2013, **135**, 10274–10277.
- 56 H. Wang, Z. Lu, S. Xu, D. Kong, J. J. Cha, G. Zheng, P.-C. Hsu, K. Yan, D. Bradshaw, F. B. Prinz and Y. Cui, *Proc. Natl. Acad. Sci. U. S. A.*, 2013, **110**, 19701–19706.
- 57 L. Liu, J. Wu, L. Wu, M. Ye, X. Liu, Q. Wang, S. Hou, P. Lu, L. Sun, J. Zheng, L. Xing, L. Gu, X. Jiang, L. Xie and L. Jiao, *Nat. Mater.*, 2018, **17**, 1108–1114.
- 58 J. Zhu, Z. C. Wang, H. Dai, Q. Wang, R. Yang, H. Yu, M. Liao, J. Zhang, W. Chen, Z. Wei, N. Li, L. Du, D. Shi, W. Wang, L. Zhang, Y. Jiang and G. Zhang, *Nat. Commun.*, 2019, **10**, 1348.
- 59 Y. Zhou, J. L. Silva, J. M. Woods, J. V. Pondick, Q. Feng, Z. Liang, W. Liu, L. Lin, B. Deng, B. Brena, F. Xia, H. Peng, Z. Liu, H. Wang, C. M. Araujo and J. J. Cha, *Adv. Mater.*, 2018, **30**, e1706076.
- 60 D. Gao, B. Xia, C. Zhu, Y. Du, P. Xi, D. Xue, J. Ding and J. Wang, *J. Mater. Chem. A*, 2018, **6**, 510–515.
- 61 S. S. Chee, H. Jang, K. Lee and M. H. Ham, *ACS Appl. Mater. Interfaces*, 2020, **12**, 31804–31809.
- 62 W. Xiao, P. Liu, J. Zhang, W. Song, Y. P. Feng, D. Gao and J. Ding, *Adv. Energy Mater.*, 2017, **7**, 1602086.
- 63 P. Liu, J. Zhu, J. Zhang, P. Xi, K. Tao, D. Gao and D. Xue, *ACS Energy Lett.*, 2017, **2**, 745–752.
- 64 Y. Luo, S. Zhang, H. Pan, S. Xiao, Z. Guo, L. Tang, U. Khan, B. F. Ding, M. Li, Z. Cai, Y. Zhao, W. Lv, Q. Feng, X. Zou, J. Lin, H. M. Cheng and B. Liu, *ACS Nano*, 2020, **14**, 767–776.
- 65 H. You, Z. Zhuo, X. Lu, Y. Liu, Y. Guo, W. Wang, H. Yang, X. Wu, H. Li and T. Zhai, *CCS Chem.*, 2019, **1**, 396–406.
- 66 Y. Yu, G. H. Nam, Q. He, X. J. Wu, K. Zhang, Z. Yang, J. Chen, Q. Ma, M. Zhao, Z. Liu, F. R. Ran, X. Wang, H. Li, X. Huang, B. Li, Q. Xiong, Q. Zhang, Z. Liu, L. Gu, Y. Du, W. Huang and H. Zhang, *Nat. Chem.*, 2018, **10**, 638–643.
- 67 M. Yan, X. Zhou, X. Pan, J. Wang, L. Xia, K. Yu, X. Liao, X. Xu, L. He and L. Mai, *Nano Res.*, 2018, **11**, 3205–3212.
- 68 C. H. Kim, Y. Wang and C. D. Frisbie, *Anal. Chem.*, 2019, **91**, 1627–1635.
- 69 W. Zhang, X. Liao, X. Pan, M. Yan, Y. Li, X. Tian, Y. Zhao, L. Xu and L. Mai, *Small*, 2019, **15**, e1900964.
- 70 H. Xiang, Y. Zheng, Y. Chen, Y. Xu, T. S. Hu, Y. Feng, Y. Zhou, S. Liu and X. Chen, *Chin. Chem. Lett.*, 2022, **33**, 3221–3226.
- 71 M. Ding, G. Zhong, Z. Zhao, Z. Huang, M. Li, H. Y. Shiu, Y. Liu, I. Shakir, Y. Huang and X. Duan, *ACS Cent. Sci.*, 2018, **4**, 590–599.



- 72 H. Yang, Q. He, Y. Liu, H. Li, H. Zhang and T. Zhai, *Chem. Soc. Rev.*, 2020, **49**, 2916–2936.
- 73 X. Zhu, C. Wang and L. Fu, *Cell Rep. Phys. Sci.*, 2020, **1**, 100190.
- 74 J. Wang, M. Yan, K. Zhao, X. Liao, P. Wang, X. Pan, W. Yang and L. Mai, *Adv. Mater.*, 2017, **29**, 1604464.
- 75 F. L. Ling, T. W. Zhou, X. Q. Liu, W. Kang, W. Zeng, Y. X. Zhang, L. Fang, Y. Lu and M. Zhou, *Nanotechnology*, 2018, **29**, 03LT01.
- 76 C. V. Nguyen, *Superlattices Microstruct.*, 2018, **116**, 79–87.
- 77 T. V. Vu, N. V. Hieu, L. T. P. Thao, N. N. Hieu, H. V. Phuc, H. D. Bui, M. Idrees, B. Amin, L. M. Duc and C. V. Nguyen, *Phys. Chem. Chem. Phys.*, 2019, **21**, 22140–22148.
- 78 Y. Wang, S. Udyavara, M. Neurock and C. D. Frisbie, *Nano Lett.*, 2019, **19**, 6118–6123.
- 79 Z. Wang, H. H. Wu, Q. Li, F. Besenbacher, Y. Li, X. C. Zeng and M. Dong, *Adv. Sci.*, 2020, **7**, 1901382.
- 80 J. Huang, Z. Zhuang, Y. Zhao, J. Chen, Z. Zhuo, Y. Liu, N. Lu, H. Li and T. Zhai, *Angew. Chem., Int. Ed.*, 2022, **61**, e202203522.
- 81 Y. Pan, X. Wang, W. Zhang, L. Tang, Z. Mu, C. Liu, B. Tian, M. Fei, Y. Sun, H. Su, L. Gao, P. Wang, X. Duan, J. Ma and M. Ding, *Nat. Commun.*, 2022, **13**, 3063.
- 82 M. Yan, X. Pan, P. Wang, F. Chen, L. He, G. Jiang, J. Wang, J. Z. Liu, X. Xu, X. Liao, J. Yang and L. Mai, *Nano Lett.*, 2017, **17**, 4109–4115.
- 83 Y. Liu, J. Guo, E. Zhu, L. Liao, S. J. Lee, M. Ding, I. Shakir, V. Gambin, Y. Huang and X. Duan, *Nature*, 2018, **557**, 696–700.
- 84 A. Allain, J. Kang, K. Banerjee and A. Kis, *Nat. Mater.*, 2015, **14**, 1195–1205.
- 85 H. Murata, Y. Nakajima, N. Saitoh, N. Yoshizawa, T. Suemasu and K. Toko, *Sci. Rep.*, 2019, **9**, 4068.
- 86 C. H. Lui, L. Liu, K. F. Mak, G. W. Flynn and T. F. Heinz, *Nature*, 2009, **462**, 339–341.
- 87 W. J. Yu, Z. Li, H. Zhou, Y. Chen, Y. Wang, Y. Huang and X. Duan, *Nat. Mater.*, 2013, **12**, 246–252.
- 88 A. Allain, J. Kang, K. Banerjee and A. Kis, *Nat. Mater.*, 2015, **14**, 1195.
- 89 C. H. Chiang, Y. C. Yang, J. W. Lin, Y. C. Lin, P. T. Chen, C. L. Dong, H. M. Lin, K. M. Chan, Y. T. Kao, K. Suenaga, P. W. Chiu and C. W. Chen, *ACS Nano*, 2022, **16**, 18274–18283.
- 90 Y. Zhou, J. V. Pondick, J. L. Silva, J. M. Woods, D. J. Hynek, G. Matthews, X. Shen, Q. Feng, W. Liu, Z. Lu, Z. Liang, B. Brena, Z. Cai, M. Wu, L. Jiao, S. Hu, H. Wang, C. M. Araujo and J. J. Cha, *Small*, 2019, **15**, e1900078.
- 91 Y. Chen, K. Yang, B. Jiang, J. Li, M. Zeng and L. Fu, *J. Mater. Chem. A*, 2017, **5**, 8187–8208.
- 92 J. Wu, *Chem. Rev.*, 2022, **122**, 10821–10859.
- 93 Y. He, Q. He, L. Wang, C. Zhu, P. Golani, A. D. Handoko, X. Yu, C. Gao, M. Ding, X. Wang, F. Liu, Q. Zeng, P. Yu, S. Guo, B. I. Yakobson, L. Wang, Z. W. she, Z. Zhang, M. Wu, Q. J. Wang, H. Zhang and Z. Liu, *Nat. Mater.*, 2019, **18**, 1098–1104.
- 94 X. Liu, B. Li, X. Li, A. R. Harutyunyan, J. Hone and D. V. Esposito, *Nano Lett.*, 2019, **19**, 8118–8124.
- 95 M. Ding, Q. He, G. Wang, H. C. Cheng, Y. Huang and X. Duan, *Nat. Commun.*, 2015, **6**, 7867.
- 96 Z. Mu, N. Han, D. Xu, B. Tian, F. Wang, Y. Wang, Y. Sun, C. Liu, P. Zhang, X. Wu, Y. Li and M. Ding, *Nat. Commun.*, 2022, **13**, 6911.
- 97 X. Zhang, M. Zhang, Y. Deng, M. Xu, L. Artiglia, W. Wen, R. Gao, B. Chen, S. Yao, X. Zhang, M. Peng, J. Yan, A. Li, Z. Jiang, X. Gao, S. Cao, C. Yang, A. J. Kropf, J. Shi, J. Xie, M. Bi, J. A. van Bokhoven, Y.-W. Li, X. Wen, M. Flytzani-Stephanopoulos, C. Shi, W. Zhou and D. Ma, *Nature*, 2021, **589**, 396–401.
- 98 N. Clark, D. J. Kelly, M. Zhou, Y.-C. Zou, C. W. Myung, D. G. Hopkinson, C. Schran, A. Michaelides, R. Gorbachev and S. J. Haigh, *Nature*, 2022, **609**, 942–947.
- 99 Y. Zhao, X.-G. Zhang, N. Bodappa, W.-M. Yang, Q. Liang, P. M. Radjenovica, Y.-H. Wang, Y.-J. Zhang, J.-C. Dong, Z.-Q. Tian and J.-F. Li, *Energy Environ. Sci.*, 2022, **15**, 3968–3977.
- 100 X. Zhou, J. Shan, L. Chen, B. Y. Xia, T. Ling, J. Duan, Y. Jiao, Y. Zheng and S.-Z. Qiao, *J. Am. Chem. Soc.*, 2022, **144**, 2079–2084.
- 101 K. Sun, X. Wu, Z. Zhuang, L. Liu, J. Fang, L. Zeng, J. Ma, S. Liu, J. Li, R. Dai, X. Tan, K. Yu, D. Liu, W.-C. Cheong, A. Huang, Y. Liu, Y. Pan, H. Xiao and C. Chen, *Nat. Commun.*, 2022, **13**, 6260.
- 102 R. Ge, Y. Wang, Z. Li, M. Xu, S. M. Xu, H. Zhou, K. Ji, F. Chen, J. Zhou and H. Duan, *Angew. Chem., Int. Ed.*, 2022, **61**, e202200211.
- 103 R. Hao, Y. Fan, M. D. Howard, J. C. Vaughan and B. Zhang, *Proc. Natl. Acad. Sci. U. S. A.*, 2018, **115**, 5878–5883.
- 104 H. Han, Q. Jacquet, Z. Jiang, F. N. Sayed, J.-C. Jeon, A. Sharma, A. M. Schankler, A. Kakekhani, H. L. Meyerheim, J. Park, S. Y. Nam, K. J. Griffith, L. Simonelli, A. M. Rappe, C. P. Grey and S. S. P. Parkin, *Nat. Mater.*, 2023, **22**, 1128–1135.
- 105 A. Yang, G. Zhou, X. Kong, R. A. Vilá, A. Pei, Y. Wu, X. Yu, X. Zheng, C.-L. Wu, B. Liu, H. Chen, Y. Xu, D. Chen, Y. Li, S. Fakra, H. Y. Hwang, J. Qin, S. Chu and Y. Cui, *Nat. Nanotechnol.*, 2020, **15**, 231–237.
- 106 B. Tian, X. Zheng, T. J. Kempa, Y. Fang, N. Yu, G. Yu, J. Huang and C. M. Lieber, *Nature*, 2007, **449**, 885–889.
- 107 M. Velický, M. A. Bissett, C. R. Woods, P. S. Toth, T. Georgiou, I. A. Kinloch, K. S. Novoselov and R. A. W. Dryfe, *Nano Lett.*, 2016, **16**, 2023–2032.
- 108 J. Zeng, X. He, S.-J. Liang, E. Liu, Y. Sun, C. Pan, Y. Wang, T. Cao, X. Liu, C. Wang, L. Zhang, S. Yan, G. Su, Z. Wang, K. Watanabe, T. Taniguchi, D. J. Singh, L. Zhang and F. Miao, *Nano Lett.*, 2018, **18**, 7538–7545.
- 109 S. Hu, M. Lozada-Hidalgo, F. C. Wang, A. Mishchenko, F. Schedin, R. R. Nair, E. W. Hill, D. W. Boukhvalov, M. I. Katsnelson, R. A. W. Dryfe, I. V. Grigorieva, H. A. Wu and A. K. Geim, *Nature*, 2014, **516**, 227–230.

